免疫調節剤の薬剤代謝およびIBD病勢予測因子としてのgenetic biomarkerの有用性に関する検討

内藤裕二、高木智久、○内山和彦（京都府立医科大学消化器内科）

炎症性腸疾患病変部におけるエピゲノム修飾の網羅的解析

○河村由紀[1]、大坪武史[1]、大島健志朗[2]、遠藤高帆[3]、豊田哲郎[3]、河村　裕[4]、小西文雄[4]、矢野秀朗[5]、斉藤幸夫[5]、服部正平[2]、土肥多惠子[1]（国立国際医療センター研究所 肝炎・免疫研究センター 消化器疾患研究部[1]、東京大学大学院新領域創成科学研究科[2]、理化学研究所生命情報基盤研究部門[3]、自治医科大学さいたま医療センター外科[4]、国立国際医療センター戸山病院外科[5]）

C-(1)-4　腸内細菌関連バイオマーカーの開発　(10:44～11:08)

総括　藤山佳秀　滋賀医科大学消化器内科

T-RFLP法を用いた小児炎症性腸疾患患者の腸内細菌叢の解析

○青松友槻[1,3]、安藤　朗[2]、今枝広丞[1]、馬場重樹[1]、辻川知之[1]、佐々木雅也[1]、井上敬介[3]、余田　篤[3]、玉井　浩[3]、藤山佳秀[1]（滋賀医科大学消化器内科[1]、滋賀医科大学大学院医学系研究科消化器免疫分野[2]、大阪医科大学小児科[3]）

新規乳酸菌由来の活性物質の慢性腸炎モデル動物による前臨床試験

○藤谷幹浩[1]、上野伸展[1]、稲場勇平[1]、岡本耕太郎[1]、盛一健太郎[1]、田邊裕貴[1]、前本篤男[23]、蘆田知史[23]、高後　裕[1]（旭川医科大学内科学講座消化器・血液腫瘍制御内科学分野[1]、旭川医科大学消化管再生修復医学講座[2]、札幌東徳洲会病院IBDセンター[3]）

う蝕病原性口腔細菌（虫歯菌）S.mutansによる炎症性腸疾患増悪の可能性とそのメカニズム・症例対照研究

中島　淳[1]、○日暮琢磨[1]、松橋信行[2]、辰巳健志[3]、杉田　昭[3]、河口貴昭[4]、高添正和[4]（横浜市立大学附属病院消化器内科[1]、NTT東日本関東病院消化器内科[2]、横浜市立市民病院炎症性腸疾患科[3]、社会保険中央総合病院炎症性腸疾患センター[4]）

C-(1)-5　炎症による発癌バイオマーカーの開発　(11:08～11:24)

総括　味岡洋一　新潟大学院医歯学総合研究科分子診断病理学分野

潰瘍性大腸炎関連大腸癌の発癌過程におけるDNA損傷応答の意義

○味岡洋一[1]、若井俊文[2]、谷　優佑[1]、山口尚之[1]、高林広明[1]（新潟大学教育研究院医歯学系分子・診断病理学[1]、新潟大学教育研究院医歯学系小児外科分野[2]）

Colitic cancerにおけるAtoh1発現の意義

○土屋輝一郎、加納嘉人、鄭　秀、堀田伸勝、根本泰宏、大島　茂、岡本隆一、永石宇司、中村哲也、渡辺　守（東京医科歯科大学消化器病態学）

C-(2)　粘膜修復機構解析と治療応用　(11:24～11:40)

総括　今井浩三　東京大学医科学研究所先端医療研究センター癌制御分野（渡辺　守）

骨髄間葉系幹細胞由来gut trophic factorの免疫学的側面（各個研究）

○永石歓和[1]、有村佳昭[2]、渡邊秀平[2]、那須野正尚[2]、苗代康可[3]、篠村恭久[2]、今井浩三[4]（札幌医科大学第二解剖[1]、札幌医科大学第一内科[2]、札幌医科大学医療人育成センター[3]、東京大学医科学研究所　先端医療研究センター　癌制御分野[4]）

大腸上皮幹細胞培養とその臨床応用技術開発

○中村哲也、油井史郎、根本泰宏、水谷知裕、鄭　秀、永石宇司、岡本隆一、土屋輝一郎、渡辺　守（東京医科歯科大学消化器病態学）

事務局連絡

閉会挨拶

(11:50終了予定)

Ⅶ.　研究成果の別刷

nature medicine

Functional engraftment of colon epithelium expanded *in vitro* from a single adult Lgr5$^+$ stem cell

Shiro Yui[1,6], Tetsuya Nakamura[2,6], Toshiro Sato[3,5], Yasuhiro Nemoto[1], Tomohiro Mizutani[1], Xiu Zheng[1], Shizuko Ichinose[4], Takashi Nagaishi[1], Ryuichi Okamoto[2], Kiichiro Tsuchiya[1], Hans Clevers[3] & Mamoru Watanabe[1]

Adult stem-cell therapy holds promise for the treatment of gastrointestinal diseases. Here we describe methods for long-term expansion of colonic stem cells positive for leucine-rich repeat containing G protein-coupled receptor 5 (Lgr5$^+$ cells) in culture. To test the transplantability of these cells, we reintroduced cultured GFP$^+$ colon organoids into superficially damaged mouse colon. The transplanted donor cells readily integrated into the mouse colon, covering the area that lacked epithelium as a result of the introduced damage in recipient mice. At 4 weeks after transplantation, the donor-derived cells constituted a single-layered epithelium, which formed self-renewing crypts that were functionally and histologically normal. Moreover, we observed long-term (>6 months) engraftment with transplantation of organoids derived from a single Lgr5$^+$ colon stem cell after extensive *in vitro* expansion. These data show the feasibility of colon stem-cell therapy based on the *in vitro* expansion of a single adult colonic stem cell.

Epithelial stem cells maintain tissue homeostasis throughout the gastrointestinal tract[1–3]. The Wnt, bone morphogenetic protein (BMP) and Notch cascades function together to regulate stem-cell maintenance[4,5]. *Lgr5* marks stem cells in small intestinal and colonic crypts[6] and in gastric units[7]. *Bmi1* may mark distinct stem cells in the proximal small intestine[8]. It has been shown that freshly isolated intestinal epithelium can be transplanted in rodents after resident epithelium has been surgically removed[9,10]. We previously developed a three-dimensional culture technique that allows expansion of single Lgr5$^+$ stem cells from small intestine[11] , stomach[7] and colon[12]. The resulting organoids then expand and self organize into an epithelial architecture that is reminiscent of that seen in *in vivo* histology. Moreover, the growing organoids maintain their tissue identity even after prolonged culture. Here we sought to evaluate whether the cultured Lgr5$^+$ cells faithfully represent the tissue-resident Lgr5$^+$ stem cells and, thus, are able to regenerate epithelial tissue *in vivo*. Considering that the colon is very vulnerable to disease in humans, we focused on colonic stem cells in our analyses.

RESULTS

Long-term, serum-free culture system for colonic organoids

We subjected the colons of adult mice to a combination of enzymes[13], reducing agents[14] and mechanical disruption. The resulting crypt fragments were mostly devoid of α smooth muscle actin gene (*Acta2*)-expression–positive non-epithelial components and consisted of a mix of cadherin 1, type 1, E-cadherin (*Cdh1*)$^+$ cells expressing terminal differentiation marker genes (*Muc2*, *CA2* and *ChgA*) and Lgr5$^+$ stem cells (**Supplementary Fig. 1a,b**).

The addition of R-spondin 1 (Rspo1), Noggin and epidermal growth factor (EGF), which are all essential to small intestine culture[11], did not maintain the growth of colonic crypts. We therefore developed the following 'TMDU (Tokyo Medical and Dental University) protocol': we embedded crypts in type I collagen in serum-free medium with Wnt3a, hepatocyte growth factor (HGF)[15,16] and BSA, in addition to Rspo1, Noggin and EGF (**Supplementary Fig. 1c**). Sequential imaging of the cultures revealed rapid growth of cystic structures (**Fig. 1a**). Wnt3a, Rspo1 and BSA were essential to this growth (**Supplementary Fig. 1d**). As predicted by previous results[17,18], Rspo1 could be substituted with Wnt3a (data not shown). Although Noggin, EGF and HGF were not essential for growth of the colonic crypts, each enhanced their growth (**Supplementary Fig. 1e**). The colonic organoids rarely had buds (**Fig. 1a**, **Supplementary Fig. 2a** and **Supplementary Video 1**). Of note, small intestinal organoids also generate cystic structures when Wnt3a is added to them[19].

The colonic organoids were single layered (**Supplementary Fig. 2b**), and all the cells within were positive for Cdh1 expression (**Fig. 1b**). The basal membranes of the organoids faced outward (**Fig. 1b**). Ki67$^+$ cells were present in the colonic organoids (**Fig. 1b**), as were alcian blue–positive goblet cells, chromogranin A (ChgA)$^+$ enteroendocrine cells, carbonic anhydrase II (CA2)$^+$ colonocytes and cytochrome c oxidase subunit I (COX1)$^+$ tuft cells[20] (**Fig. 1b**). Transmission electron microscopy revealed epithelial characteristics such as microvilli (**Fig. 1c**) and junctional complexes (**Fig. 1d**) in the organoids. However, stromal cells were absent (**Supplementary Fig. 2c**). Mitotic cells with condensed chromosomes were present in the organoids (**Fig. 1e**), and goblet cells (**Fig. 1f**) and enteroendocrine cells (**Fig. 1g**) could also be clearly detected.

[1]Department of Gastroenterology and Hepatology, Graduate School, Tokyo Medical and Dental University, Bunkyo-ku, Tokyo, Japan. [2]Department of Advanced Therapeutics for Gastrointestinal Diseases, Tokyo Medical and Dental University, Bunkyo-ku, Tokyo, Japan. [3]Hubrecht Institute and University Medical Centre, Utrecht, The Netherlands. [4]Research Center for Medical and Dental Sciences, Tokyo Medical and Dental University, Bunkyo-ku, Tokyo, Japan. [5]Present address: Department of Gastroenterology, Keio University School of Medicine, Shinjuku-ku, Tokyo, Japan. [6]These authors contributed equally to this work. Correspondence should be addressed to H.C. (h.clevers@hubrecht.eu) or M.W. (mamoru.gast@tmd.ac.jp).

Received 30 July 2011; accepted 29 November 2011; published online 11 March 2012; doi:10.1038/nm.2695

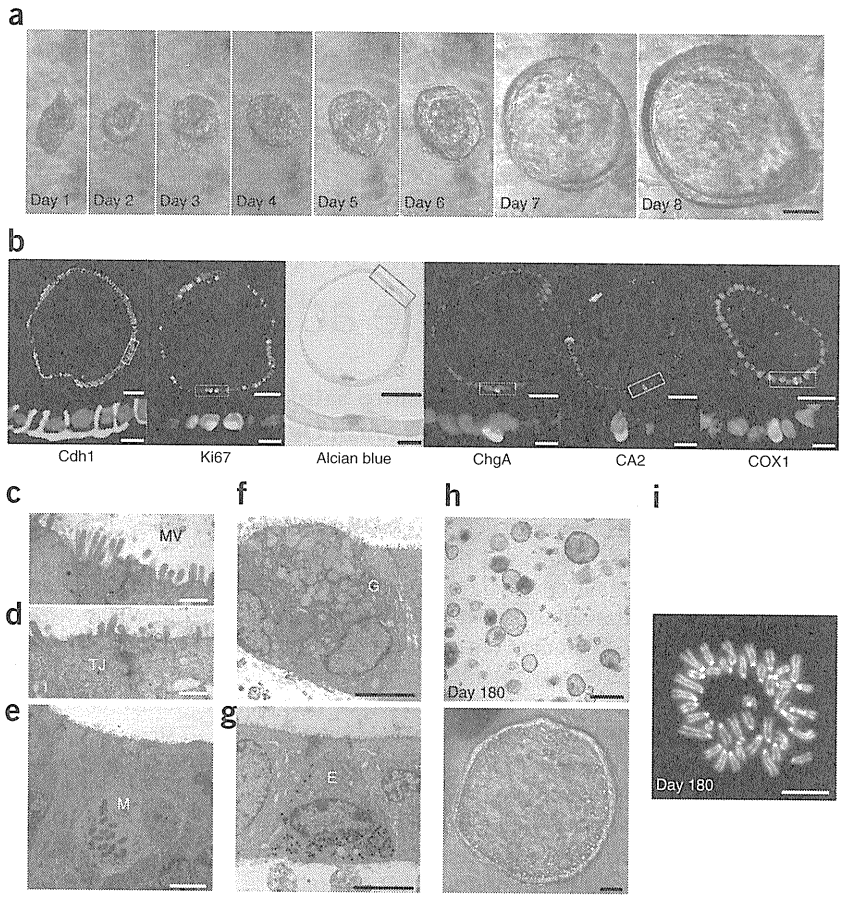

Figure 1 Long-term, serum-free culture of colonic epithelial cells. (**a**) A representative colonic crypt growing as a cystic structure. Scale bar, 50 μm. Time-lapse images of another colonic crypt are shown in **Supplementary Figure 2a** and **Supplementary Video 1**. (**b**) Histology of the colonic organoids at day 8 of culture. Cdh1$^+$ cells, actively proliferating Ki67$^+$ cells (green) and terminally differentiated cells stained with alcian blue (blue, goblet cells) or immunostained with ChgA (green, enteroendocrine cells), CA2 (green, colonocytes) or COX1 (green, tuft cells) are shown. Higher magnification views of the boxed areas are shown at the bottom. DAPI staining was performed, except for the experiments in which we performed alcian blue staining. Scale bars, top, 50 μm; bottom, 10 μm. (**c**–**g**) Transmission electron microscopy analysis for organoids at day 8. (**c**,**d**) Microvilli (MV) and intracellular tight junctions (TJ) are shown. (**e**) Mitotic (M) cells showing chromatin condensation. (**f**,**g**) Goblet cells (G) with mucus granules (**f**) and enteroendocrine cells (E) with electron dense granules (**g**) are shown. Scale bars: **c**,**d**, 0.5 μm; **e**–**g**, 5 μm. Low-power views of **f** and **g** are also shown in **Supplementary Figure 2c**. (**h**) The culture at day 180 (top) and its representative organoid (bottom). Scale bars, top, 500 μm; bottom, 50 μm. Images of the growth of a single cell after passage are shown in **Supplementary Figure 3** and **Supplementary Video 2**. (**i**) Metaphase spread of a cell at day 180 shows a normal karyotype ($2n = 40$). Scale bar, 10 μm.

The organoids could be passaged weekly at a 1:2 ratio (**Supplementary Fig. 3** and **Supplementary Video 2**). Addition of the Rho kinase inhibitor Y-27632 (ref. 21) improved the replating efficiency of the organoids[11]. We successfully propagated organoids for more than 6 months without clear alterations of morphology (**Fig. 1h**) or karyotype (**Fig. 1i**).

Lgr5$^+$ cells are enriched in colonic organoids

We tracked the expression of *Lgr5* over 60 d and found a substantial elevation during the first 8 d of observation (**Fig. 2a**). We found no change in the expression of *ChgA* and *CA2*, whereas *Muc2* expression was repressed in the first 8 d (**Fig. 2a**). Addition of a combination of Wnt3a, Rspo1 and BSA induced *Lgr5* expression (**Fig. 2b**). *Lgr5* expression was further upregulated by the addition of Noggin, which is an antagonist of BMP[22] (**Fig. 2b**). The Notch pathway suppresses the

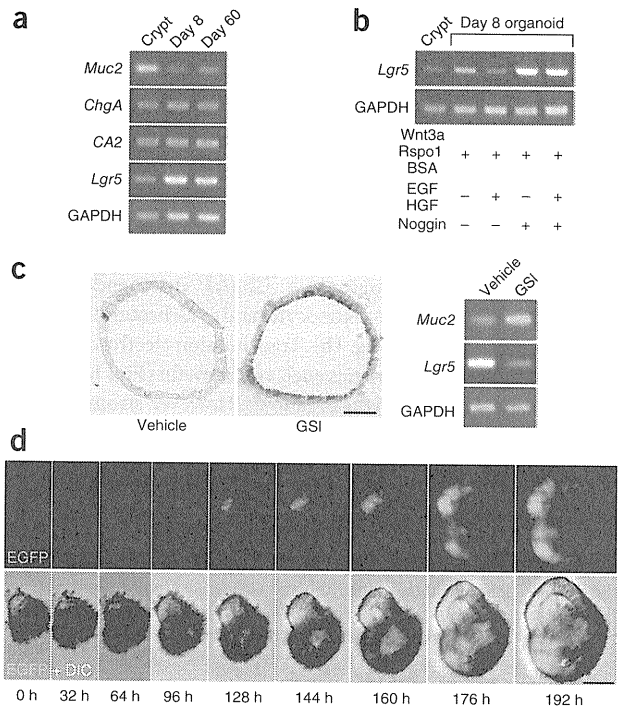

Figure 2 Lgr5$^+$ stem cells are enriched in cultured organoids. (**a**) RT-PCR analysis of the colonic crypts immediately after isolation (crypt) or organoids cultured for 8 or 60 d. *Lgr5* was upregulated and stayed constant thereafter. Differentiation marker genes (*Muc2*, *ChgA* and *CA2*) were expressed over 60 d. The primers used are listed in **Supplementary Table 1**. (**b**) RT-PCR shows that *Lgr5* upregulation is mediated by a combination of minimum factors (Wnt3a, Rspo1 and BSA) and Noggin but not by EGF and HGF. (**c**) Notch signal-mediated cell fate determination *in vitro*. Cultured organoids were treated with GSI, LY-411575 or vehicle alone from day 4 to day 8. Organoids stained with alcian blue are shown (left). Scale bar, 50 μm. RT-PCR shows that the expression of *Muc2* is upregulated, whereas the expression of *Lgr5* is reciprocally downregulated in organoids treated with LY-411575 (GSI, right). Similar results were obtained in three independent experiments, and representative data are shown. (**d**) A time-lapse imaging of a growing colonic crypt obtained from an *Lgr5-EGFP-ires-CreERT2* mouse over 192 h. The top panel shows EGFP and the bottom panel shows merged images of EGFP and differential interference contrast (DIC). Scale bar, 50 μm. The corresponding video (**Supplementary Video 3**) and similar results from another example are available as **Supplementary Figure 4a** and **Supplementary Video 4**.

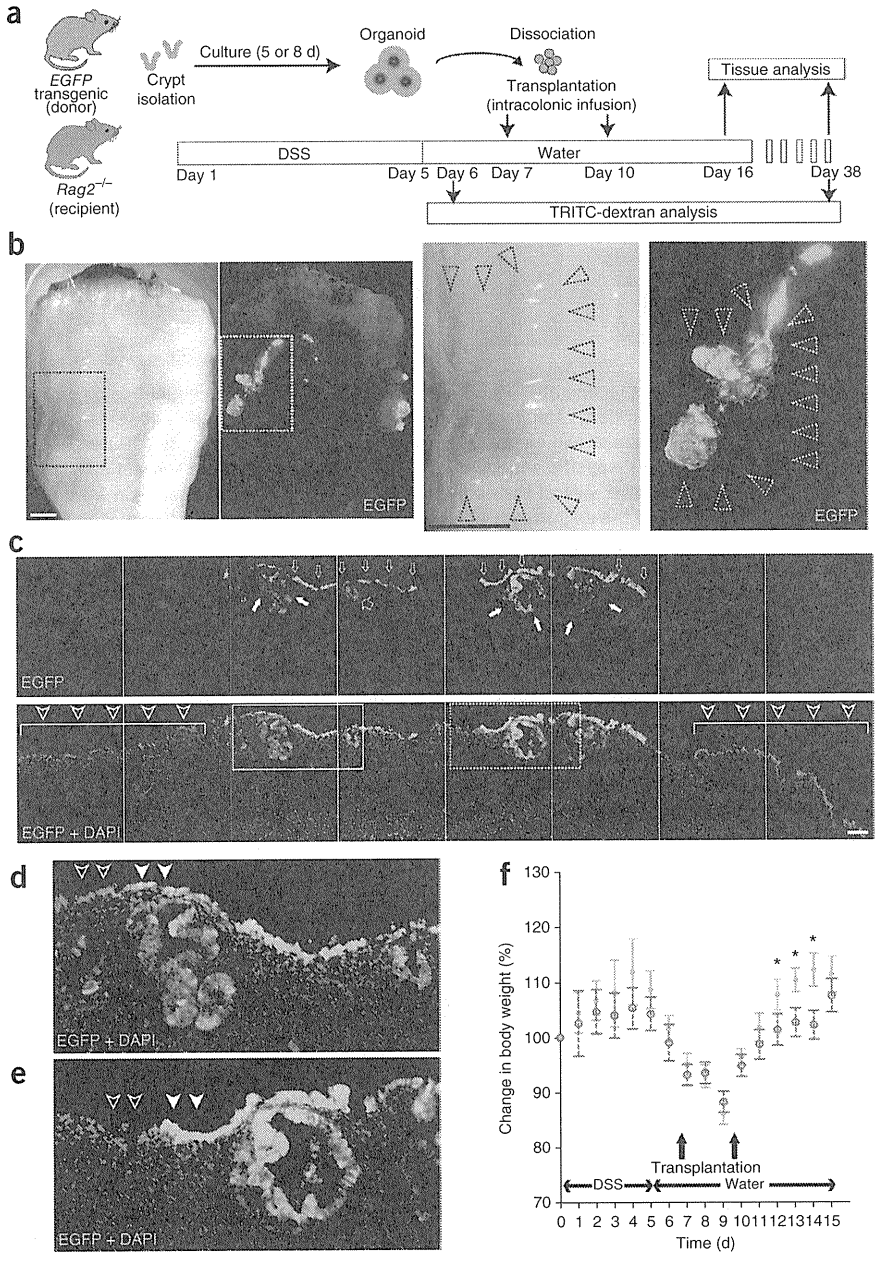

Figure 3 Transplantation of cultured cells improves acute colitis. (**a**) Experimental protocols. (**b**) Recipient colon at 6 d after transplantation. Low-power views (stereoscopic and fluorescent images) are shown on the left. High-power views of the areas in the dotted squares are shown in the right. The black dotted arrowheads show a depressed area surrounded by edematous mucosa. EGFP$^+$ areas overlapping the damaged region (white dotted arrowheads) are also shown. Note that the outline of the tissue is not precisely the same in the stereoscopic and fluorescent images, as they were acquired on different microscopes. Scale bars, 1 mm. (**c**) Histology of the EGFP$^+$ area shown in **b**. EGFP (top) and the merged image with DAPI staining (bottom). EGFP$^+$ cells cover the damaged mucosa that intervene separate areas preserving crypt structures (bottom, arrowheads). EGFP$^+$ cells constitute flat linings (top, narrow open arrow) or an invagination (top, wide open arrows), the latter of which is reminiscent of crypts. EGFP$^+$ cystic structures were also observed in the EGFP$^+$ cells (top, filled white arrows). The regions in the solid- and dotted-line boxes are shown at higher magnification in **d** and **e**, respectively. Scale bar, 100 μm. (**d**) High-power view of the solid box in **c**. (**e**) High-power view of the dotted box in **c**. (**f**) *Rag2*$^{-/-}$ mice were given DSS for 5 d, and then transplantation ($n = 6$) or sham-transplantion ($n = 6$) was performed. On day 16, the presence of engraftment was retrospectively assessed after the mice were killed. The body weights of the mice with EGFP$^+$ engraftment (green squares, $n = 4$) and sham-transplanted controls (red open circles, $n = 6$) are presented as a percentage of their initial weight. Error bars, s.e.m. $^*P < 0.05$ (Student's t test).

differentiation of progenitors[23,24] and stem cells[25] toward secretory lineages. We treated the colonic organoids with LY-411575, a γ-secretase inhibitor (GSI) that is capable of inhibiting Notch signaling[26,27]. Notch inhibition induced a goblet-cell phenotype with an increased level of *Muc2* mRNA and a reciprocal decrease in the expression of *Lgr5* (**Fig. 2c**).

We next performed live imaging of colonic organoids obtained from *Lgr5-EGFP-internal ribosome entry site (ires)-CreERT2* mice[6] in which an enhanced GFP (EGFP) and tamoxifen-inducible Cre recombinase cassette is integrated into the *Lgr5* locus. The *Lgr5*-promoter–driven EGFP expression initially stayed at a marginal level but then increased beginning at day 5 (**Fig. 2d**, **Supplementary Fig. 4a** and **Supplementary Videos 3** and **4**). We confirmed the expansion of Lgr5$^+$ cells at a single-cell resolution (**Supplementary Fig. 4b**). Over multiple passages, the *Lgr5-EGFP* locus tended to become silenced, whereas the wild-type *Lgr5* allele remained active (**Fig. 2a**,**b**). Taken together, colonic Lgr5$^+$ stem cells were able to self renew and expand *in vitro*.

Cultured colonic organoids rescue damaged epithelium

We next tested the transplantability of the cultured organoids (**Fig. 3a**). We induced colonic mucosal damage by providing immunocompromised *Rag2*$^{-/-}$ mice with colitis-inducing dextran sulfate sodium (DSS)[28] for 5 d. Most of the mice developed acute colitis characterized by weight loss, bloody stool, diarrhea and epithelial injury in the distal colon. At 7 and 10 d after initiating DSS administration, we dissociated the organoids cultured from *EGFP* transgenic mice[29] into small fragments, suspended them in a Matrigel-containing PBS and instilled them by enema in recipient mice.

At 16 d after the start of DSS administration, the recipient colons showed varying degrees of recovery. Multiple EGFP$^+$ areas appeared as well-demarcated patches in the treated colons (**Fig. 3b**). We did not observe any EGFP$^+$ areas in colons not treated with DSS (data not shown). Histologically, the EGFP$^+$ cells covered the submucosa and were located between the less damaged recipient tissues (**Fig. 3c**). The EGFP$^+$ cells formed flat or slightly invaginated linings (**Fig. 3c**). We also observed large cystic EGFP$^+$ structures below the surface of the treated colons (**Fig. 3c**). Some of the EGFP$^+$ areas connected to the recipients' epithelium (**Fig. 3d**), whereas others repopulated areas that were devoid of recipient epithelium (**Fig. 3e**). Notably, the body weights of the mice with engraftment were

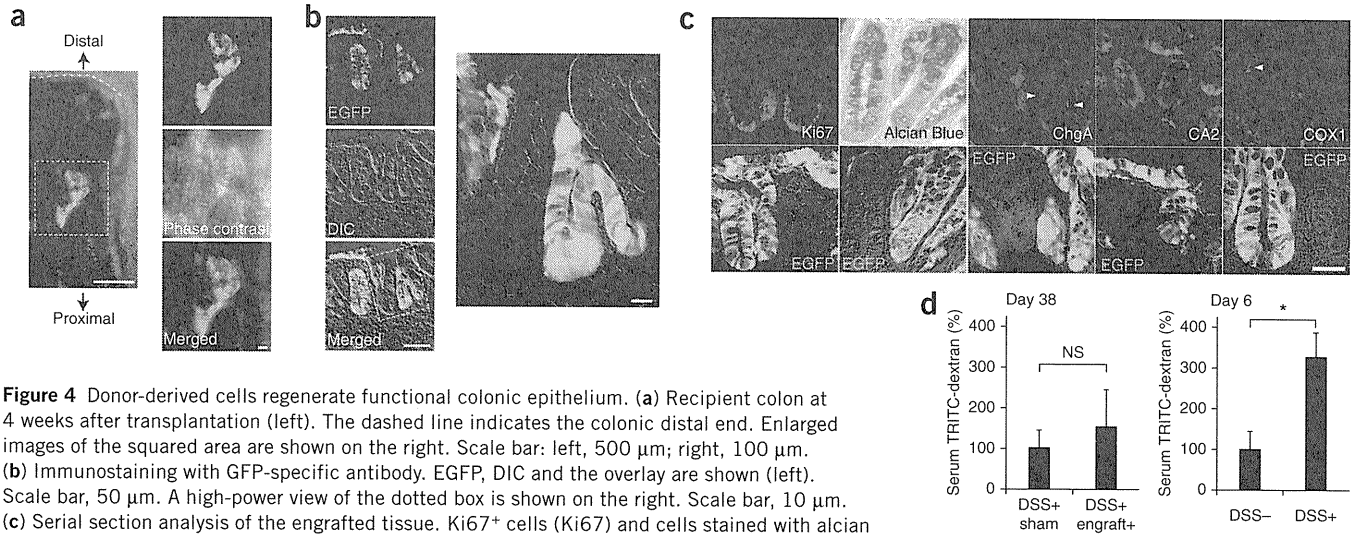

Figure 4 Donor-derived cells regenerate functional colonic epithelium. (**a**) Recipient colon at 4 weeks after transplantation (left). The dashed line indicates the colonic distal end. Enlarged images of the squared area are shown on the right. Scale bar: left, 500 μm; right, 100 μm. (**b**) Immunostaining with GFP-specific antibody. EGFP, DIC and the overlay are shown (left). Scale bar, 50 μm. A high-power view of the dotted box is shown on the right. Scale bar, 10 μm. (**c**) Serial section analysis of the engrafted tissue. Ki67$^+$ cells (Ki67) and cells stained with alcian blue (goblet cells) or immunostained for ChgA, CA2 and COX1 are shown. Images are shown with or without DAPI staining. The bottom row shows neighboring sections stained for GFP. Arrowheads point to ChgA$^+$ or COX1$^+$ cells. Scale bar, 50 μm. (**d**) After DSS colitis induction, transplantation ($n = 6$) or sham transplantation ($n = 6$) was performed. Mice were administered TRITC-dextran by gavage before killing on day 38. Four out of six colons in the transplanted group had EGFP$^+$ engraftment, and the serum TRITC concentration in these mice is shown (DSS+ engraft+; $n = 4$) as a percentage of that in the sham-transplanted group (DSS+ sham; $n = 6$). As a control, DSS colitis was induced (DSS+; $n = 6$) or uninduced (DSS–; $n = 6$) in *Rag2*$^{-/-}$ mice, and these mice were subjected for the same assay on day 6 without transplantation. Data are shown as a percentage of the concentrations in uninduced mice. Error bars, s.e.m. $^*P < 0.05$, NS, not significant (Student's *t* test).

higher than those of sham-transplanted mice (**Fig. 3f**; with statistically significant results at days 12, 13 and 14, $P < 0.05$).

At 4 weeks after transplantation, tube-like EGFP$^+$ crypts appeared in the distal colon (**Fig. 4a**) that were morphologically indistinguishable from the surrounding EGFP$^-$ epithelium (**Fig. 4b**). Notably, the engrafted crypts were entirely EGFP$^+$, indicating the presence of EGFP$^+$ stem cells (**Fig. 4b**). Cells in the lower part of the EGFP$^+$ crypts were normally Ki67$^+$, and the EGFP$^+$ crypts contained all

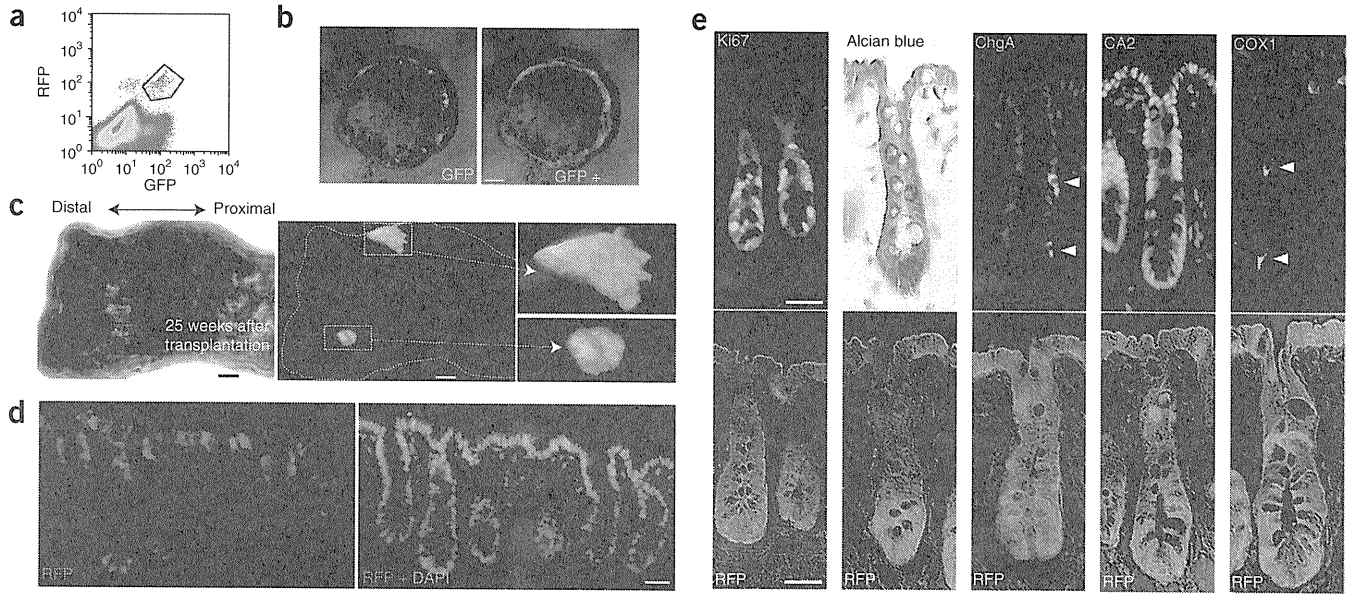

Figure 5 Single Lgr5$^+$ stem-cell–derived cultured cells serve as long-lived, multipotential stem cells *in vivo*. (**a**) Fluorescence-activated cell sorting analysis of colonic cells of *R26R-Confetti* mice crossed with *Lgr5-EGFP-ires-CreERT2* mice 3 d after Cre induction. The EGFP$^+$ and RFP$^+$ populations located in the box were sorted and cultured. (**b**) Images are shown of one out of four organoids grown from sorted single Lgr5$^+$ cells at day 6. EGFP$^+$ stem cells are scattered in the organoid (left), with all the offspring being positive for RFP (right). Scale bar, 50 μm. (**c**) Images of the recipient colon at 25 weeks after transplantation. The phase-contrast view of the recipient colon is shown on the left. The fluorescent image shows the tissue contains RFP$^+$ grafts (right). Scale bar, 1 mm. Enlarged images of the boxed areas are also shown (2.7-fold magnification). (**d**) Immunostaining of the RFP$^+$ engraft at 25 weeks after transplantation. An image of RFP-specific antibody staining (left) and an image of RFP staining merged with DAPI staining (right) are shown. Scale bar, 50 μm. (**e**) Serial section analysis of the engrafted RFP$^+$ tissue at 25 weeks after transplantation. The top panels show Ki67, alcian blue, ChgA, CA2 or COX1 staining with or without nuclei stained by DAPI. The bottom panels show the adjacent sections stained for RFP. Arrowheads point to ChgA$^+$ enteroendocrine cells and COX1$^+$ tuft cells. Scale bars, 50 μm.

terminally differentiated cell types (**Fig. 4c**). We probed the epithelial permeability of the engrafts using tetramethylrhodamine isothiocyanate (TRITC)-conjugated dextran (TRITC-dextran). Blood TRITC concentrations in transplanted mice were comparable to those in control mice, indicating a maintenance of epithelial barrier function in these engrafts (**Fig. 4d**). Notably, transplantation was less successful with freshly isolated donor cells ($P < 0.05$, Mann-Whitney U test; **Supplementary Fig. 5**), suggesting that the expansion of stem cells during the culture is associated with a higher success rate of transplantation. In addition, Matrigel-containing organoid suspensions transplanted better than organoids suspended in PBS (**Supplementary Fig. 5**; $P < 0.05$, Mann-Whitney U test), proposing a role for the simultaneous supply of extracellular matrix in successful transplantation.

Engraftment of organoids derived from a single Lgr5$^+$ cell

We next sought to initiate the protocol described above from a single stem cell (**Supplementary Fig. 6a**). We crossed *Lgr5-EGFP-ires-CreERT2* mice with *R26R-Confetti* reporter mice[30]. In the resulting offspring, tamoxifen-induced Cre activation resulted in Cre-mediated recombination at the *Rosa26* locus in individual Lgr5$^+$ stem cells, leading to stochastically selected expression of one out of four fluorescent proteins: red fluorescent protein (RFP), cyan fluorescent protein (CFP), GFP or yellow fluorescent protein (YFP). At 3 d after Cre activation, we sorted cells double positive for Lgr5-EGFP and Confetti-RFP, which consisted of ~0.02% of the total cells (**Fig. 5a**), equivalent to ~100 cells per mouse.

We cultured the sorted cells after a limiting dilution (100 cells per 96 well) using the Hubrecht protocol (Online Methods; protocol described previously[12] with addition of Y-27632 in the first 2 d). Four stem cells double positive for Lgr5-EGFP and Confetti-RFP grew out, which was comparable to the culture efficiency of small intestinal stem cells[11] (**Fig. 5b**). Organoids were expanded to more than 100 wells in >10 weeks, frozen and shipped. After thawing, we recovered the cells under the TMDU protocol. We transplanted ~500 organoids per recipient mouse, as described above. Analyses at 4, 17, 21 and 25 weeks after transplantation revealed the presence of grafts in these mice (**Fig. 5c** and **Supplementary Figs. 6b,c** and **7a**). At 25 weeks after transplantation, RFP$^+$ cells still generated a single-layered epithelium. We noted no sign of adenomatous or dysplastic change in any of the transplanted areas (**Fig. 5d**). Again, all differentiated cell types, as well as Ki67$^+$ proliferating cells, were present at normal ratios (**Fig. 5e** and **Supplementary Fig. 7b**).

DISCUSSION

Here we describe methodologies to isolate, culture and transplant Lgr5$^+$ colon stem cells. Our observations confirm that *Lgr5* marks genuine stem cells that retain their self-renewal and multilineage-differentiation properties even after prolonged culture. A major difference between small-intestinal and colon-culture conditions is in the latter's requirement for Wnt. Although Wnt factors can initiate Wnt signals on their own, R-spondins (such as Rspo1) can only augment preexisting Wnt signals[31]. Because Paneth cells produce Wnt3, they serve as the center of organization of the stem cell niche[19]. At the colon crypt bottoms, secretory cells are located between the Lgr5$^+$ stem cells that—like Paneth cells—express CD24 (ref. 19). However, these CD24$^+$ secretory cells do not produce a sufficient amount of Wnt proteins *in vitro* (data not shown). Therefore, colon organoids cannot grow from Rspo1 alone but, rather, also require exogenous Wnt.

This study provides proof of principle that cultured Lgr5$^+$ cells can be used for stem-cell therapy to repair damaged epithelium. Transplanted cells adhere to and cover superficially damaged tissue. Further, engrafted recipient mice had higher body weights than ungrafted controls, implying a beneficial role for the donor cells in DSS-induced acute colitis. Although further optimization is clearly needed, the current study implies that *in vitro* expansion and transplantation of gastrointestinal stem cells may be a promising option for patients with severe gastrointestinal epithelial injuries.

Lgr5$^+$ stem cells divide once every day *in vivo*[6], thus defying the Hayflick limit[32]. They appear similarly unrestricted in their proliferative capacity *in vitro*, while they retain their original tissue identity. It is of interest that the Lgr5 protein is now known to reside in the Wnt receptor complex to function as a receptor for Rspo1 (refs. 33,34), which is a crucial component of long-term organoid culture systems that we have developed. As the resulting organoids have now been proven to be transplantable, the Lgr5$^+$ stem cell isolation and expansion technology may provide a simple and safe avenue for the development of new regenerative and gene-therapy strategies.

METHODS

Methods and any associated references are available in the online version of the paper at http://www.nature.com/naturemedicine/.

Note: Supplementary information is available on the Nature Medicine website.

ACKNOWLEDGMENTS

We thank M. Okabe (Osaka University) for EGFP transgenic mice and Y. Kato, J. Inazawa, I. Sekiya (TMDU), H. Snippert and R. Vries (Hubrecht Institute) for technical assistance. This study was supported by Grant-in-Aid for Scientific Research from the Japanese Ministry of Education, Culture, Sports, Science and Technology, by the Health and Labour Sciences Research Grants for Research on Intractable Diseases from Ministry of Health, Labour and Welfare of Japan, and by a grant from the European Research Council and from the Dutch Cancer Foundation.

AUTHOR CONTRIBUTIONS

T. Nakamura, H.C. and M.W. designed the study. S.Y., T. Nakamura and T.S. performed experiments and analyzed data. T. Nakamura, T.S. and H.C. wrote the paper. Y.N., T. Nagaishi and K.T. assisted in transplantation experiments. T.M., X.Z. and K.T. gave support in gene analysis. R.O. helped with the immunohistochemistry. S.I. advised on the electron microscopy. H.C. and M.W. gave conceptual advice and supervised the project.

COMPETING FINANCIAL INTERESTS

The authors declare competing financial interests: details accompany the full-text HTML version of the paper at http://www.nature.com/naturemedicine/.

Published online at http://www.nature.com/naturemedicine/.
Reprints and permissions information is available online at http://www.nature.com/reprints/index.html.

1. Potten, C.S., Booth, C. & Pritchard, D.M. The intestinal epithelial stem cell: the mucosal governor. *Int. J. Exp. Pathol.* **78**, 219–243 (1997).
2. Bjerknes, M. & Cheng, H. Intestinal epithelial stem cells and progenitors. *Methods Enzymol.* **419**, 337–383 (2006).
3. Barker, N., van de Wetering, M. & Clevers, H. The intestinal stem cell. *Genes Dev.* **22**, 1856–1864 (2008).
4. Crosnier, C., Stamataki, D. & Lewis, J. Organizing cell renewal in the intestine: stem cells, signals and combinatorial control. *Nat. Rev. Genet.* **7**, 349–359 (2006).
5. Radtke, F. & Clevers, H. Self-renewal and cancer of the gut: two sides of a coin. *Science* **307**, 1904–1909 (2005).
6. Barker, N. *et al.* Identification of stem cells in small intestine and colon by marker gene *Lgr5*. *Nature* **449**, 1003–1007 (2007).
7. Barker, N. *et al.* Lgr5^{+ve} stem cells drive self-renewal in the stomach and build long-lived gastric units *in vitro*. *Cell Stem Cell* **6**, 25–36 (2010).
8. Sangiorgi, E. & Capecchi, M.R. *Bmi1* is expressed *in vivo* in intestinal stem cells. *Nat. Genet.* **40**, 915–920 (2008).
9. Avansino, J.R., Chen, D.C., Woolman, J.D., Hoagland, V.D. & Stelzner, M. Engraftment of mucosal stem cells into murine jejunum is dependent on optimal dose of cells. *J. Surg. Res.* **132**, 74–79 (2006).
10. Tait, I.S., Evans, G.S., Flint, N. & Campbell, F.C. Colonic mucosal replacement by syngeneic small intestinal stem cell transplantation. *Am. J. Surg.* **167**, 67–72 (1994).

11. Sato, T. *et al.* Single Lgr5 stem cells build crypt-villus structures *in vitro* without a mesenchymal niche. *Nature* **459**, 262–265 (2009).
12. Sato, T. *et al.* Long-term expansion of epithelial organoids from human colon, adenoma, adenocarcinoma, and Barrett's epithelium. *Gastroenterology* **141**, 1762–1772 (2011).
13. Booth, C., Patel, S., Bennion, G.R. & Potten, C.S. The isolation and culture of adult mouse colonic epithelium. *Epithelial Cell Biol.* **4**, 76–86 (1995).
14. Whitehead, R.H., Demmler, K., Rockman, S.P. & Watson, N.K. Clonogenic growth of epithelial cells from normal colonic mucosa from both mice and humans. *Gastroenterology* **117**, 858–865 (1999).
15. Kanayama, M. *et al.* Hepatocyte growth factor promotes colonic epithelial regeneration via Akt signaling. *Am. J. Physiol. Gastrointest. Liver Physiol.* **293**, G230–G239 (2007).
16. Tahara, Y. *et al.* Hepatocyte growth factor facilitates colonic mucosal repair in experimental ulcerative colitis in rats. *J. Pharmacol. Exp. Ther.* **307**, 146–151 (2003).
17. Kim, K.A. *et al.* Mitogenic influence of human R-spondin1 on the intestinal epithelium. *Science* **309**, 1256–1259 (2005).
18. Wei, Q. *et al.* R-spondin1 is a high affinity ligand for LRP6 and induces LRP6 phosphorylation and β-catenin signaling. *J. Biol. Chem.* **282**, 15903–15911 (2007).
19. Sato, T. *et al.* Paneth cells constitute the niche for Lgr5 stem cells in intestinal crypts. *Nature* **469**, 415–418 (2011).
20. Gerbe, F. *et al.* Distinct ATOH1 and Neurog3 requirements define tuft cells as a new secretory cell type in the intestinal epithelium. *J. Cell Biol.* **192**, 767–780 (2011).
21. Watanabe, K. *et al.* A ROCK inhibitor permits survival of dissociated human embryonic stem cells. *Nat. Biotechnol.* **25**, 681–686 (2007).
22. Haramis, A.P. *et al. De novo* crypt formation and juvenile polyposis on BMP inhibition in mouse intestine. *Science* **303**, 1684–1686 (2004).
23. Fre, S. *et al.* Notch signals control the fate of immature progenitor cells in the intestine. *Nature* **435**, 964–968 (2005).
24. van Es, J.H. *et al.* Notch/γ-secretase inhibition turns proliferative cells in intestinal crypts and adenomas into goblet cells. *Nature* **435**, 959–963 (2005).
25. van Es, J.H., de Geest, N., van de Born, M., Clevers, H. & Hassan, B.A. Intestinal stem cells lacking the Math1 tumour suppressor are refractory to Notch inhibitors. *Nat. Commun.* **1**, 18 (2010).
26. Wong, G.T. *et al.* Chronic treatment with the γ-secretase inhibitor LY-411,575 inhibits β-amyloid peptide production and alters lymphopoiesis and intestinal cell differentiation. *J. Biol. Chem.* **279**, 12876–12882 (2004).
27. Okamoto, R. *et al.* Requirement of Notch activation during regeneration of the intestinal epithelia. *Am. J. Physiol. Gastrointest. Liver Physiol.* **296**, G23–G35 (2009).
28. Wirtz, S., Neufert, C., Weigmann, B. & Neurath, M.F. Chemically induced mouse models of intestinal inflammation. *Nat. Protoc.* **2**, 541–546 (2007).
29. Okabe, M., Ikawa, M., Kominami, K., Nakanishi, T. & Nishimune, Y. 'Green mice' as a source of ubiquitous green cells. *FEBS Lett.* **407**, 313–319 (1997).
30. Snippert, H.J. *et al.* Intestinal crypt homeostasis results from neutral competition between symmetrically dividing Lgr5 stem cells. *Cell* **143**, 134–144 (2010).
31. Binnerts, M.E. *et al.* R-Spondin1 regulates Wnt signaling by inhibiting internalization of LRP6. *Proc. Natl. Acad. Sci. USA* **104**, 14700–14705 (2007).
32. Hayflick, L. & Moorhead, P.S. The serial cultivation of human diploid cell strains. *Exp. Cell Res.* **25**, 585–621 (1961).
33. de Lau, W. *et al.* Lgr5 homologues associate with Wnt receptors and mediate R-spondin signalling. *Nature* **476**, 293–297 (2011).
34. Carmon, K.S., Gong, X., Lin, Q., Thomas, A. & Liu, Q. R-spondins function as ligands of the orphan receptors LGR4 and LGR5 to regulate Wnt/β-catenin signaling. *Proc. Natl. Acad. Sci. USA* **108**, 11452–11457 (2011).

ONLINE METHODS

Mice. *Rag2*$^{-/-}$ mice were from Taconic Farms and Central Laboratories for Experimental Animals. *EGFP* transgenic mice[29], *Lgr5-EGFP-ires-CreERT2* mice[6] and *R26R-Confetti* mice[30] are described elsewhere. Male and female mice were randomly used for all experiments. All animal experiments were performed with the approval of the Institutional Animal Care and Use Committee of TMDU.

TMDU protocol for crypt isolation and three-dimensional culture. The colonic tissue was minced and digested. The crypts were further purified by mechanical disruption and density gradient centrifugation. A total of 2,000 crypts were suspended in 200 µl of the collagen type I solution (Nitta Gelatin Inc.) and placed in 48-well plates. After polymerization, 500 µl of Advanced DMEM/F12 containing BSA (Sigma), mouse EGF (mEGF) (PeproTech), mWnt3a, mRspo1, mHGF and mNoggin (all from R&D Systems) was added (TMDU medium). For passage, the gel was digested, and then the organoids were disaggregated with EDTA. The dissociated organoids were mixed in type I collagen solution and used for culture. A Rho kinase inhibitor, Y-27632, was added for the first 2 d after the cells were propagated. Where indicated, to induce goblet cell differentiation, organoids were treated with LY-411575, a GSI. See details in the **Supplementary Methods**.

Chromosome analysis. Chromosome karyotyping was performed according to a standard protocol as detailed in the **Supplementary Methods**.

Stereomicroscopy, phase-contrast imaging and histology. Images were acquired on either a fluorescence microscope equipped with phase-contrast setting (BZ-8000, KEYENCE), a fluorescent stereomicroscope system MVX10 (Olympus) or a fluorescence microscope DeltaVision system (Applied Precision). For histology and immunohistochemistry, tissues and organoids were fixed, sequentially dehydrated in sucrose in PBS, and frozen in OCT compound (Tissue Tek). Cryosections were examined by conventional H&E, alcian blue staining and a spectrum of immunohistochemical reactions, as detailed in the **Supplementary Methods**.

Transmission electron microscopy. Transmission electron microscopy was performed in a standard fashion and is detailed in the **Supplementary Methods**.

Live imaging. Live imaging was performed on the DeltaVision system. A culture dish placed on the microscope stage was covered with a chamber in which a humidified premixed gas consisting of 5% CO_2 and 95% air was infused, and the whole setup was set at 37 °C. DIC and fluorescent images were acquired at 20-min intervals. The data were processed using Softworx (Applied Precision) and, if necessary, image editing was performed using Adobe Photoshop Elements 7.0.

Semi-quantitative RT-PCR. Semi-quantitative RT-PCR was performed in standard fashion. The primer sequences used are listed in **Supplementary Table 1**. PCR products were separated on agarose gels and visualized using ImageQuant TL system (GE Healthcare).

Sorting and Hubrecht-protocol culture for single Lgr5$^+$ cells. Tamoxifen was injected into *R26R-Confetti* mice crossed with *Lgr5-EGFP-ires-CreERT2* mice, and the colonic crypts from the resulting mice were isolated 3 d later. Epithelial cells were dissociated with TrypLE express (Invitrogen) and analyzed by MoFlo (DakoCytomation). Viable single cells were gated, and then the cells doubly positive for EGFP and RFP were sorted and embedded in Matrigel (BD Bioscience) on 96-well plates. An Advanced DMEM/F12 culture medium supplemented with penicillin and streptomycin, 4-(2-hydroxyethyl)-1-piperazineethanesulfonic acid (HEPES), glutamax, N2, B27 (all from Invitrogen) and growth factors (EGF, noggin and R-spondin) was diluted 1:1 with Wnt3a-conditioned medium and used as Hubrecht medium. Y-27632 was included for the first 2 d to avoid anoikis. Growth factors were added every other day, and the entire medium was changed every 4 d. See the **Supplementary Methods** for additional details.

Transplantation experiments. For the EGFP$^+$ cell transplantations, cells isolated from colon tissues were cultured for 5 or 8 d according to the TMDU protocol and used as donor cells. For single Lgr5$^+$-cell–derived organoid transplantation, cells were expanded based on the Hubrecht protocol and then cryopreserved. The cells were then shipped, thawed and further cultured. Acute colitis was induced by feeding 6-week-old *Rag2*$^{-/-}$ mice with 3.0% DSS (molecular weight 10,000; Ensuiko Sugar Refining Co.) dissolved in drinking water for 5 d (days 1–5). At 7 and 10 d after the start of DSS administration, donor cells equivalent to those from ~500 organoids were instilled into colonic lumen as a suspension. After infusion, the anal verge was glued for 6 h. After the transplantation on day 10, mice were maintained as usual before they were killed and analyzed. See the **Supplementary Methods** for additional details.

TRITC-dextran permeability assay. Intestinal permeability was assessed by enteral administration of TRITC-dextran (molecular mass 4.4 kDa; Sigma). Transplanted or sham-transplanted mice were gavaged with TRITC-dextran 4 h before killing on day 38. Whole blood was obtained at the time of killing, and then the colonic tissues were examined for whether the EGFP$^+$ engrafts were present. TRITC-dextran measurements were performed on an ARVO MX (PerkinElmer), with serial dilutions of TRITC-dextran used as a standard curve.

Statistical analyses. Data are shown as means ± s.e.m. Data for **Figures 3f**, **4d** and **Supplementary Figure 7b** were statistically analyzed by the two-sample Student's *t* test. The data for **Supplementary Figure 5** showed non-normal distributions and were analyzed by Mann-Whitney *U* test. Statistical significance for comparisons was assigned at $P < 0.05$.

Additional methods. Detailed methodology is described in the **Supplementary Methods**.

Biochemical and Biophysical Research Communications xxx (2012) xxx–xxx

Contents lists available at SciVerse ScienceDirect

Biochemical and Biophysical Research Communications

journal homepage: www.elsevier.com/locate/ybbrc

Real-time analysis of P-glycoprotein-mediated drug transport across primary intestinal epithelium three-dimensionally cultured *in vitro*

Tomohiro Mizutani [a,1], Tetsuya Nakamura [b,*,1], Ryo Morikawa [a], Masayoshi Fukuda [a], Wakana Mochizuki [a], Yuhki Yamauchi [a], Kengo Nozaki [a], Shiro Yui [a], Yasuhiro Nemoto [a], Takashi Nagaishi [a], Ryuichi Okamoto [b], Kiichiro Tsuchiya [a], Mamoru Watanabe [a]

[a] Department of Gastroenterology and Hepatology, Graduate School, Tokyo Medical and Dental University, 1-5-45 Yushima, Bunkyo-ku, Tokyo 113-8519, Japan
[b] Department of Advanced Therapeutics for GI Diseases, Graduate School, Tokyo Medical and Dental University, 1-5-45 Yushima, Bunkyo-ku, Tokyo 113-8519, Japan

ARTICLE INFO

Article history:
Received 30 January 2012
Available online xxxx

Keywords:
P-glycoprotein
Drug transport
Intestinal absorption
Cell membrane permeability
Primary culture
Live imaging

ABSTRACT

P-glycoprotein (P-gp) is an efflux transporter that regulates bioavailability of orally administered drugs at the intestinal epithelium. To develop an *in vitro* experimental model that mimics P-gp-mediated intestinal drug transport *in vivo*, we employed normal intestinal epithelium three-dimensionally cultured. Physiological expression of P-gp mRNA and the expression of its protein at the apical membrane were observed in the small intestinal epithelium grown as cystic organoids. Rhodamine123 (Rh123), a substrate for P-gp, was actively transported in the basoapical direction and accumulated in the luminal space, while the epithelial integrity was kept intact. Furthermore, we were able to monitor the whole process of Rh123 transport and its inhibition by verapamil in real-time, from which kinetic parameters for Rh123 transport could be estimated by a mathematical modeling. The method here described to evaluate the dynamics of P-gp-mediated transport in primary intestinal epithelial cells would be instrumental in investigating the physiological function of P-gp and its inhibitors/inducers *in vitro*.

1. Introduction

Bioavailability of many clinically relevant drugs is modulated by the activity of efflux transporters expressed in the epithelial lining of the intestine [1,2]. P-glycoprotein (P-gp, also known as ABCB1), a member of the ATP-binding cassette family of transporters, is located in the apical membrane of intestinal epithelial cells [3,4] and serves as an important determinant of the disposition of many orally administered drugs [5–9]. There is, thus, a considerable interest in predicting the P-gp-mediated elimination of drug candidates and assessing the drug-drug interactions involving P-gp substrates and inhibitors/inducers in the intestinal epithelium.

Various model systems have been reported to assess the intestinal epithelial drug transport *in vitro*. Among these, cell based assays using human tumor-derived cell lines, such as Caco-2 cells, are the most commonly used method in many laboratories [10]. When grown on a membrane placed between two chambers, those cells form a well-polarized monolayer joined by tight junctions, providing a selective barrier that can be used to study influx (from the apical to the basal) and efflux (from the basal to the apical) transport of P-gp substrates [11–14]. Although such cell based systems have been well characterized and used as standard assays, several factors, such as variable expression of P-gp in those immortalized cell lines, are known to cause inter-experimental variability of the data [15,16]. Therefore, it would be of importance to develop an experimental model in which drug transport can be assessed in a reliable manner relevant to the physiological *in vivo* function of intestinal epithelium.

Recently, the long-awaited method for *in vitro* culture of normal intestinal epithelium has been developed [17]. When isolated and placed three-dimensionally, the intestinal crypts keep proliferating, forming enclosed structures with their upper openings closed. These "organoids" are lined by an epithelial monolayer containing both immature cells and terminally differentiated cells, with their apical membranes facing the luminal space inside. In light of this, we were particularly interested in determining whether this newly developed culture technology could be adapted for use in drug transport analysis.

In the present study, by developing a real-time imaging system and its mathematical modeling, we show that the primary culture of small intestinal epithelium would serve as an efficient tool to evaluate the dynamics of P-gp-mediated drug transport.

* Corresponding author. Fax: +81 3 5803 0268.
E-mail address: nakamura.gast@tmd.ac.jp (T. Nakamura).
[1] These authors contributed equally.

0006-291X/$ - see front matter © 2012 Elsevier Inc. All rights reserved.
doi:10.1016/j.bbrc.2012.01.155

Please cite this article in press as: T. Mizutani et al., Real-time analysis of P-glycoprotein-mediated drug transport across primary intestinal epithelium three-dimensionally cultured *in vitro*, Biochem. Biophys. Res. Commun. (2012), doi:10.1016/j.bbrc.2012.01.155

2. Materials and methods

2.1. 3D culture of intestinal epithelium

Culture of intestinal epithelium was performed as described previously [17]. Crypts of proximal small intestine were obtained from adult C57BL/6 mice and purified. They were counted and embedded in Matrigel (BD Biosciences) at 10,000 crypts/ml. For conventional culture, 30 μl of Matrigel was seeded on 24-well plates. For live imaging experiments, 60 μl of Matrigel was placed on 40-mm coverslips placed in 60-mm culture dishes. After the Matrigel solidified, advanced DMEM/F12 medium (Invitrogen) containing 20 ng/ml EGF (Peprotech), 100 ng/ml Noggin, 500 ng/ml R-spondin1 (R&D systems), 2 mM L-glutamine (GIBCO) and penicillin/streptomycin was overlaid. The medium was changed every 4 days. When necessary, Rh123, FITC-dextran, or verapamil (Sigma–Aldrich) was added to the medium as indicated. Animal experiments were performed with the approval of the Institutional Animal Care and Use Committee of Tokyo Medical and Dental University.

2.2. Semi-quantitative RT-PCR

Organoids were isolated from the Matrigel using BD Cell recovery solution as instructed by the manufacturer. Total RNA was isolated and 300 ng was used for cDNA synthesis in a 21 μl of reaction. 1 μl of cDNA was amplified by PCR in a 25 μl reaction. Sense (S) and antisense (AS) primers, and the cycle numbers for the amplification of each gene were as follows: S: 5'-TGCTGTGATTTTCCAGAACA-3' and AS: 5'-TCCAACATATTCGGCTTTAG-3' for Abcb1a (22 cycles); and S: 5'-CTGGCCAAGGTCATCCATGA-3' and AS: 5'-GCCATGAGGTCCACCACCCTG-3' for Gapdh (19 cycles). PCR products were separated on agarose gels and visualized using Image Quant TL system (GE Healthcare).

2.3. Immunohistochemistry

Tissues and organoids were fixed, dehydrated in 20% sucrose/PBS, and frozen in OCT compound (Tissue Tek). Cryosections (6 μm thick) were immunostained with an anti-Mdr antibody (1 μg/ml, Santa Cruz Biotechnology) and a fluorescent secondary antibody (Alexa Fluor 588, Molecular Probes). The sections were also counterstained with DAPI (Vector Laboratories) to visualize nuclei. Images were acquired on a fluorescence microscope DeltaVision system (Applied Precision).

2.4. Live imaging

The isolated crypts were mixed with Matrigel and placed on 40-mm glass coverslips so that the whole gel would be as thin as possible (<1 mm). On Day 3, the coverslip was incorporated into the FCS-2 closed cell chamber (Bioptechs), the thickness of which was set at 1 mm. The chamber was fixed on the stage of a DeltaVision microscope system covered with a thermally-controlled enclosure set at 37 °C. Spherical organoids with diameters of around 50 μm were chosen and imaged using a fluorescent microscope IX-71 (Olympus) equipped with a xenon light source, a UplansApo 10x objective (0.4 numerical aperture), a 490/20-nm excitation filter, a 528/38-nm filter, and a Cool Snap ES2 digital camera (Roper Scientific). Differential interference contrast (DIC) and fluorescent images were acquired at 3 min intervals. Exposure times were 0.2 s for DIC and 0.03 s for fluorescent images, respectively, with 1 × 1 binning and an image size of 512 × 512 pixels. These conditions were kept throughout all experiments. Immediately after the third time frame of imaging (6 min after the start), 5 ml of pre-warmed medium containing Rh123 (1 μM), with or without various concentration of verapamil, was rapidly infused from one port on the side of the chamber, allowing the preexisting medium inside to direct out of the chamber from the other side. This enabled a rapid replenishment of medium with no disturbance of the position or morphology of the organoids. All experiments were performed for 5 h and 30 min.

2.5. Data analysis and mathematical modeling

Images at individual time points of all organoids were quantitatively assessed using the SoftWoRx (Applied Precision). For individual images, circular areas with a diameter of 30 μm were manually set inside (luminal space) and outside (culture medium) of the organoid, and the fluorescent signal for each compartment was expressed by average pixel values of the circular area. The outer intensities (culture medium) of the images acquired immediately before (0 μM) and after (1 μM) the Rh123 addition were applied for calculating the concentration of all other areas of a given experiment.

For mathematical modeling, we made an assumption that Rh123 concentration in the lumen is determined only by active inward transport and passive bidirectional diffusion, both of which take place at the inner apical membrane. When Rh123 concentration (1 μM) remains stable in the donor side due to the excessively large volume in space, the rate of active transport in the basal to apical direction, V_{in} (nmol/s), can be expressed as below:

$$V_{in} = P_{app.active} \cdot S \cdot C_{out} \tag{1}$$

In this equation (Eq. (1)), $P_{app.active}$ (cm/s) is the apparent permeability coefficient of active basoapical transport, S (cm^2) is the area of inner surface of the organoids, and C_{out} (μmol/litter; nmol/cm^3) is the outer concentration of Rh123 given as 1. Passive diffusion of Rh123 can occur in both directions, depending on the concentration gradient across the apical membrane. When V_{out} (nmol/s) is defined as the rate of diffusion in the apical to basal direction, it is derived from an equation,

$$V_{out} = P_{app.passive} \cdot S \cdot (C_{in}(t) - C_{out}) \tag{2}$$

where $P_{app.passive}$ (cm/s) is the apparent permeability coefficient of bidirectional passive diffusion, S (cm^2) is the inner surface area, and C_{in} (nmol/cm^3) is the luminal Rh123 concentration that can be defined as a function of time t. The total amounts of Rh123, transported across the apical membrane inward and outward by a given time t, can be expressed as integral functions $Q_{in}(t)$ and $Q_{out}(t)$, respectively.

$$Q_{in}(t) = \int_0^t V_{in} dt = V_{in} \cdot t \tag{3}$$

$$Q_{out}(t) = \int_0^t V_{out} dt \tag{4}$$

Eq. (1) and (2) can be substituted into Eq. (3) and (4), respectively, to convert equations as below:

$$Q_{in}(t) = P_{app.active} \cdot S \cdot C_{out} \cdot t \tag{5}$$

$$Q_{out}(t) = P_{app.passive} \cdot S \cdot \int_0^t C_{in}(t) dt - P_{app.passive} \cdot S \cdot C_{out} \cdot t \tag{6}$$

The luminal spatial volume, Vol (cm^3), can be assumed to stay unchanged during the imaging and, thus, C_{in} (t) can also be expressed as below:

$$C_{in}(t) = \frac{Q_{in}(t) - Q_{out}(t)}{Vol} \tag{7}$$

From Eq. (5)–(7), C_{in} (t) can now be solved as a function of the variable t.

Please cite this article in press as: T. Mizutani et al., Real-time analysis of P-glycoprotein-mediated drug transport across primary intestinal epithelium three-dimensionally cultured *in vitro*, Biochem. Biophys. Res. Commun. (2012), doi:10.1016/j.bbrc.2012.01.155

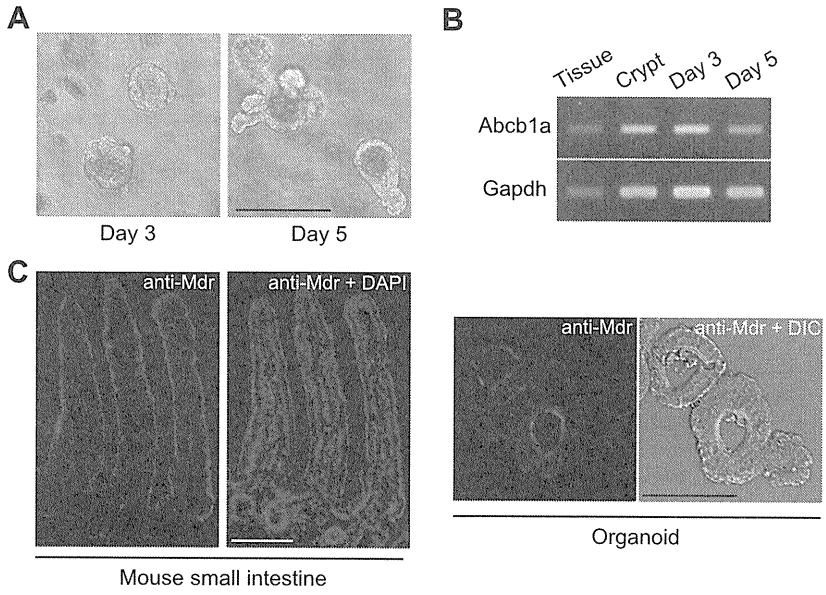

Fig. 1. Physiological expression of P-gp in cultured small intestinal organoids. (A) Phase contrast images of small intestinal organoids on Day 3 (left) and Day 5 (right) of culture. Scale bar, 100 μm. (B) Expression of P-gp (*Abcb1a*) mRNA analyzed by semi-quantitative RT-PCR. Expression levels in the whole small intestine (tissue), isolated crypts (crypt), and the organoids on Day 3 and Day 5 are shown (top). PCR products for *Gapdh* are shown as internal controls (bottom). (C) Localization of P-gp proteins. Immunohistochemistry with an anti-Mdr antibody was performed for mouse proximal small intestine tissue (mouse small intestine) and cultured organoids on Day 3 (organoid). Scale bars, 100 μm.

$$C_{in}(t) = \frac{P_{app.active} + P_{app.passive}}{P_{app.passive}} \cdot C_{out} + e^{-P_{app.passive} \cdot \frac{S}{Vol} t} \cdot \left(C_{in}(0) - \frac{P_{app.active} + P_{app.passive}}{P_{app.passive}} \cdot C_{out} \right) \quad (8)$$

The inner Rh123 concentrations calculated from the fluorescent intensities of each experiment were plotted and then fitted to the function characterized in Eq. (8) using curve fitting on MATLAB software (The MathWorks, Inc.). By applying this process to the dataset obtained from each organoid, we could retrieve two kinetic parameters A (nmol/cm^3) and B (s^{-1}) as indicated below:

$$A = \frac{P_{app.acitve} + P_{app.passive}}{P_{app.passive}} \cdot C_{out} \quad (9)$$

$$B = P_{app.passive} \cdot \frac{S}{Vol} \quad (10)$$

Substituting $4\pi r^2$ and $4\pi r^3/3$ (r denotes the radius of organoid) into S and Vol, respectively, $P_{app.active}$ and $P_{app.passive}$ could be finally determined as below:

$$P_{app.passive} = \frac{B \cdot r}{3} \quad (11)$$

$$P_{app.active} = \frac{A - C_{out}}{C_{out}} \cdot P_{app.passive} = \frac{r}{3} \cdot B \cdot \frac{A - C_{out}}{C_{out}} \quad (12)$$

2.6. Statistical analysis

Data were presented as means ± s.e. Statistical analysis was performed using the Student's t-test or Welch's t-test (Fig. 4C). Statistical significance for comparisons was assigned at $P < 0.01$ (Fig. 4C).

3. Results

First we assessed the expression of P-gp in intestinal epithelium obtained from murine small intestine and three-dimensionally cultured. As previously described [17], they grew as epithelial organoids showing round cystic structures on Day 3, and then formed asymmetric structures having growing crypt-like protrusions on Day 5 (Fig. 1A). In the mouse, P-gp is encoded by two genes, Abcb1a and Abcb1b. We could detect the expression of Abcb1a in the intestinal tissue by our semi-quantitative RT-PCR (Fig. 1B), while Abcb1b mRNA was hardly detectable even with a high number of amplification cycles (data not shown). This supported the previous finding that Abcb1a is the major species of P-gp expressed in the small intestine [18]. In the cultured organoids, expression of Abcb1a stayed unchanged on Day 3 compared with that of isolated crypts on Day 1, whereas a slight decrease in its expression was noted on Day 5 (Fig. 1B). We also tested the expression of P-gp protein. Immunostaining with an antibody,

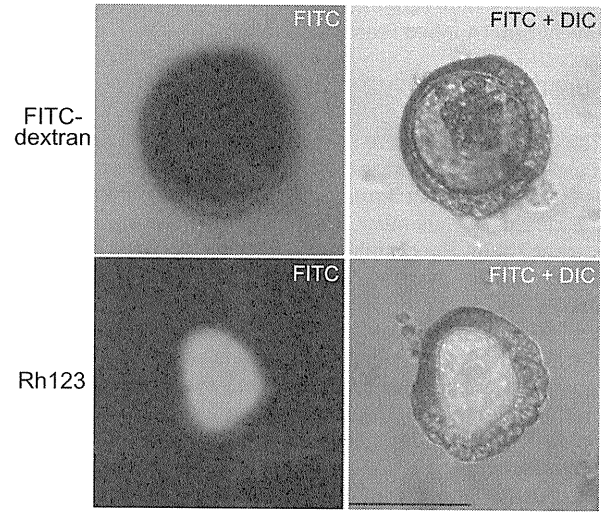

Fig. 2. Cultured organoids actively transport Rh123, while keeping their epithelial integrity. FITC-dextran (2mM, top) or Rh123 (1 μM, bottom) was added to the culture medium on Day 3, and images were acquired 5 h after the addition of the fluorescent probes. Fluorescent images (FITC) and their merged ones with DIC (FITC + DIC) are shown. Scale bar, 100 μm.

Please cite this article in press as: T. Mizutani et al., Real-time analysis of P-glycoprotein-mediated drug transport across primary intestinal epithelium three-dimensionally cultured *in vitro*, Biochem. Biophys. Res. Commun. (2012), doi:10.1016/j.bbrc.2012.01.155

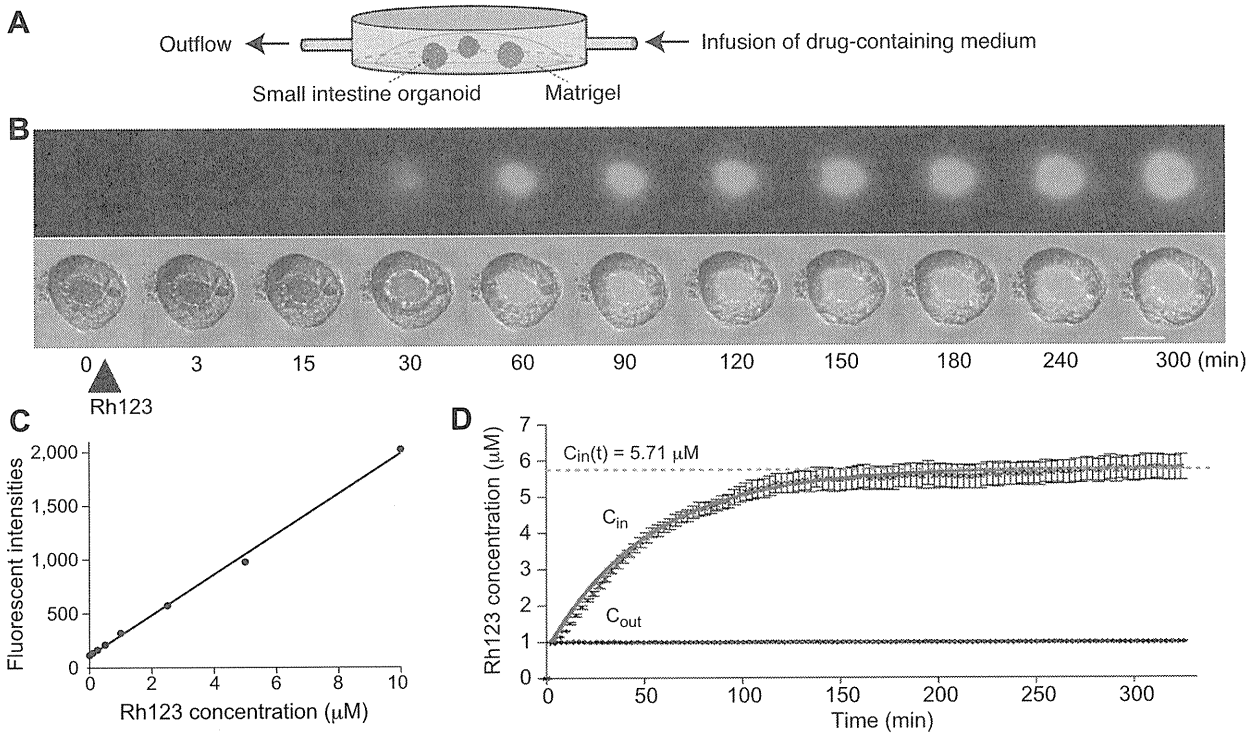

Fig. 3. Dynamics of Rh123 transport by cultured organoids and its mathematical modeling. (A) A schematic representation of the closed perfusable micro-observation chamber used for the time-lapse imaging. (B) Still images from time series of a Day 3 organoid actively transporting Rh123. Time 0 denotes the time frame immediately before the perfusion of Rh123. Fluorescent (FITC) images and their merged ones with DIC (FITC + DIC) are shown. Scale bar, 50 μm. The whole images can be viewed as Supplementary Video 1. (C) The linear correlation between the fluorescent intensity (expressed in arbitrary units) and Rh123 concentration under cell-free condition of the same experimental setting. (D) Rh123 concentrations inside and outside of organoids were calculated from data obtained by time-lapse experiments and plotted as mean ± s.e. (n = 10). A curve obtained by fitting a mathematical model to data is shown in red. (For interpretation of the references to colour in this figure legend, the reader is referred to the web version of this article.)

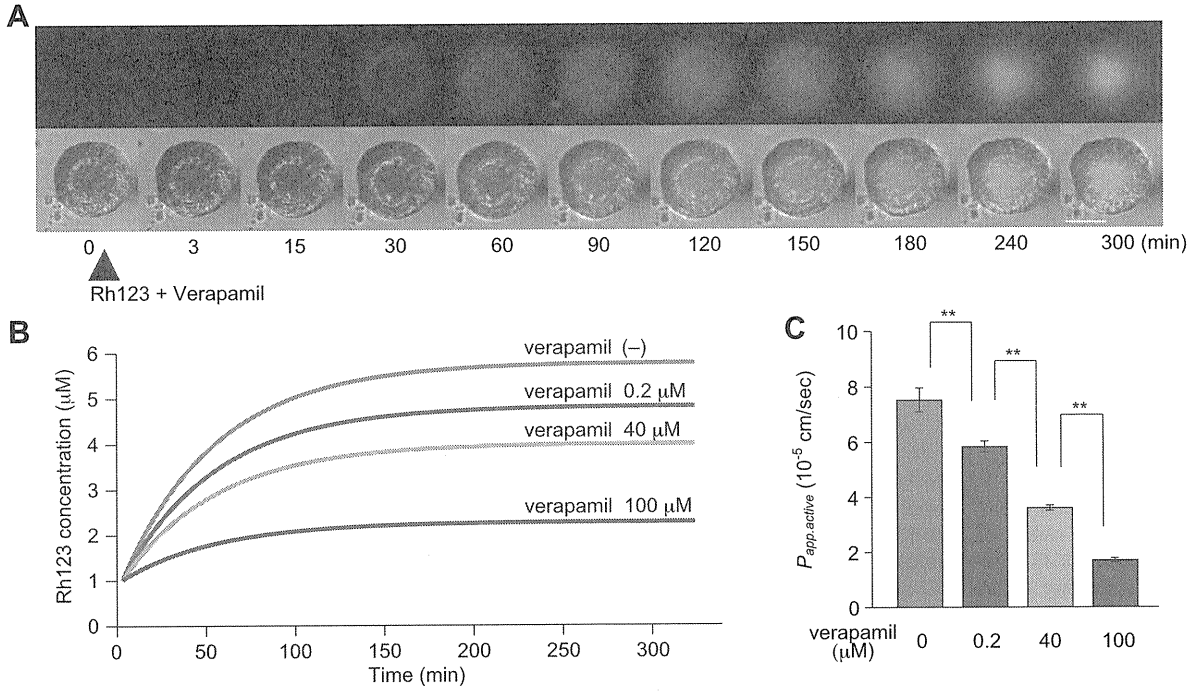

Fig. 4. Verapamil inhibits Rh123 transport across primary intestinal epithelium. (A) Time-lapse imaging experiments were performed as described in Fig. 3 in the presence of 40 μM verapamil. Fluorescent (FITC) and merged (FITC + DIC) images of a representative movie are shown. Scale bar, 50 μm. The video including these data, and other videos of the representative organoids recorded in the presence of 0.2 and 100 μM verapamil can be viewed as Supplementary Videos 2–4. (B) The curves obtained by fitting the mathematical model to data of verapamil inhibition experiments. (C) The $P_{app.active}$ values at various doses of verapamil were calculated and shown as mean ± s.e. (n = 10 for each) $^{**}P < 0.01$.

Please cite this article in press as: T. Mizutani et al., Real-time analysis of P-glycoprotein-mediated drug transport across primary intestinal epithelium three-dimensionally cultured *in vitro*, Biochem. Biophys. Res. Commun. (2012), doi:10.1016/j.bbrc.2012.01.155

capable of labeling Abcb1a on the apical surface of epithelium in the small intestinal tissue (Fig. 1C), revealed predominant expression of the transporter on the inner surface of cultured organoids on Day 3 (Fig. 1C). These results showed that the intestinal epithelial cells maintain physiological expression level and correct localization of P-gp in primary culture.

When the medium was supplemented with FITC-dextran of 4 kDa on Day 3 of culture, its fluorescent signals were excluded from the lumen even at 5 h after the supplementation (Fig. 2, top). This indicated the preservation of epithelial integrity not allowing paracellular flux of this well-characterized permeability probe. Meanwhile, Rh123, a fluorescent dye known as a substrate of P-gp [13,19,20], showed a different behavior. Its intense fluorescent signals were observed in the lumen 5 h after the addition with a stark contrast against those in outer space of organoids (Fig. 2, bottom). This clearly showed that the intestinal organoids in culture are able to conduct active transepithelial transport of Rh123 in the basal to apical direction, and the involvement of P-gp in this process was strongly suggested.

To assess the dynamics of basoapical transport of Rh123, we developed an experimental system where the whole process could be visualized in real-time (Fig. 3A). On Day 3 of culture, the organoids were placed in a micro-observation chamber having a perfusable space inside, and the ones having spherical structures with diameters of around 50 μm were chosen for imaging. The time-lapse imaging at 3 min intervals was initiated, and then the whole culture medium was replaced with Rh123 (1 μM)-containing medium immediately after the image acquisition of the third time frame (referred to as time 0 hereafter).

The fluorescent intensity of the area outside of organoids rose by the first time frame after the perfusion (3 min), indicating the rapid diffusion of Rh123 throughout the optical chamber (Fig. 3B). The luminal signals were at a comparable level to the outer signals by this time point, and then rapidly went up far exceeding the signals outside. Thereafter, this upward trend gradually declined and the enrichment of Rh123 in the inner space appeared to approach a steady-state level (Fig. 3B, Supplementary Video 1). Based on the finding that the measured fluorescent intensity was linearly correlated with Rh123 concentration under the cell-free condition of the same experimental setting (Fig. 3C), we could calculate both inner and outer concentrations of Rh123 at individual time frames for all organoids (Fig. 3D). Rh123 concentration outside stayed nearly constant, assumably because the large excess of outer spatial volume made the loss of Rh123 into the lumen almost negligible (Fig. 3D).

In order to obtain several kinetic parameters of Rh123 transport, we constructed a mathematical model on the assumption that Rh123 concentration in the tightly-closed lumen was determined only by two mechanisms at the apical cell membrane: active inward transport and passive bidirectional diffusion (See Section 2). Analysis of the dataset ($n = 10$) by the mathematical function based on this simplified two-compartment model provided a well-fitted curve (Fig. 3D, red). From this, we could extract two parameters as defined in Materials and Methods (Eq. (9) and (10)). As a result, when the observed organoids were all assumed to be spheres with a radius of 25 μm, $P_{app.active}$ and $P_{app.passive}$ were calculated as $7.53 \pm 0.45 \times 10^{-5}$ cm/s and $1.63 \pm 0.08 \times 10^{-5}$ cm/s, respectively, according to Eq. (11) and (12). Importantly, given the Eq. (8), the limit of function $C_{in}(t)$ (as t approaches infinity) could be expressed as follows:

$$\lim_{t\to\infty} C_{in}(t) = \frac{P_{app.active} + P_{app.passive}}{P_{app.passive}} \cdot C_{out} \tag{13}$$

Indeed, when $P_{app.active}$ and $P_{app.passive}$ were substituted with the values described above and C_{out} was regarded as a constant value of 1 μM, the obtained limit value of 5.71 μM represented the concentration toward which the observed C_{in} was approaching (Fig. 3D). In addition, using this model with data analysis, the ratio of basoapical active transport and bidirectional passive diffusion, $P_{app.active}/P_{app.passive}$, could be determined as around 4.6-fold, independently of the radius of organoids, r.

To assess the involvement of P-gp in Rh123 transport, we also performed time-lapse experiments where Rh123 was infused together with different doses (0.2, 40 and 100 μM) of verapamil, an inhibitor for P-gp [11,12,19]. The initial rate of transport as well as the steady-state level of the luminal Rh123 in later phases was obviously suppressed in the presence of verapamil at each dose (Fig. 4A, Supplementary Videos 2–4). According to a simple assumption that verapamil would not affect $P_{app.passive}$, we could obtain the fitting curves (Fig. 4B) by mathematical modeling of the data ($n = 10$ for each dose of verapamil), which again allowed quantitative estimates for kinetic parameters. The derived $P_{app.active}$ indicated that 40 μM of verapamil had ~50% inhibitory effect on Rh123 transport under this experimental condition (Fig. 4C).

4. Discussion

In this study, we have developed an experimental system to investigate P-gp-mediated drug transport across the small intestinal epithelium in primary culture. To date, many attempts have been made to assess the permeability of normal intestine *in vitro* including the use of excised intestinal tissues with or without the underlying submucosal layers. However, the common disadvantage of such approach has been the limited viability of intestinal tissues when isolated [16]. By contrast, as represented by Caco-2 cells, immortal cell lines have been extensively used, partly due to the ease with which the cells can be cultured. Many studies have shown the correlation between *in vitro* permeability values in Caco-2 assays and parameters of *in vivo* absorption [21–24]. However, it is pointed out that variability of the results may exist across experiments, due to the heterogeneity of the cells resulting from the phenotypic drift during the culture under different conditions. In this regard, the most distinctive feature of our system is the use of purified, non-transformed intestinal epithelial cells keeping their physiological expression and localization of P-gp. We also showed that Rh123 transport was inhibited by verapamil, indicating the functional involvement of P-gp in this process. Such availability of primary intestinal epithelium for transport assays would build a basis for a variety of application including the screening of inducers/inhibitors of P-gp in normal intestinal cells, or assessing the P-gp function in individual human specimens.

Another key feature of the presented method is its simple and rapid procedure. In the Caco-2 cell system, drugs are added to one side of the cell layer and their appearance in the other side is quantitatively measured. Experiments to calculate permeability in both directions are needed, and then P-gp-mediated transport is suggested when a higher basoapical permeability is observed [11–13]. On the other hand, even with a simple unidirectional assessment, spatial characteristics of the organoids in the present system, having tightly closed space inside, provided an intuitive information as to whether the net rate of inward transport exceeds that of outward diffusion by the luminal accumulation of fluorescence. In addition, taking advantage of time-lapse imaging and mathematical modeling, we could quantitatively estimate the ratio of basoapical active transport and bidirectional passive diffusion ($P_{app.active}/P_{app.passive}$). From Eq. (13), this ratio can also be expressed as below:

$$\frac{P_{app.active}}{P_{app.passive}} = \frac{\lim_{t\to\infty} C_{in}(t)}{C_{out}} - 1 \tag{14}$$

Please cite this article in press as: T. Mizutani et al., Real-time analysis of P-glycoprotein-mediated drug transport across primary intestinal epithelium three-dimensionally cultured *in vitro*, Biochem. Biophys. Res. Commun. (2012), doi:10.1016/j.bbrc.2012.01.155

This further indicates that the parameter $P_{app.active}/P_{app.passive}$ would be simply estimated when the ratio of inner versus outer drug concentration at an equilibrium state is obtained.

In conclusion, we have described a simple, rapid and efficient method to evaluate the dynamics of P-gp-mediated transport in normal intestinal epithelium *in vitro*. This system would be instrumental in investigating the physiological function and screening of inhibitors/inducers of P-gp and, thus, serve as a novel tool to study the bioavailability of drugs via the intestinal epithelium.

Acknowledgments

We sincerely thank Marc-Aurele Brun for his help and contribution to mathematical modeling and curve fit analysis. This study was supported by Grant-in-Aid for Scientific Research from the Japanese Ministry of Education, Culture, Sports, Science and Technology, and by Health and Labor Sciences Research Grants for Research on Intractable Diseases from the Ministry of Health, Labor and Welfare of Japan.

Appendix A. Supplementary data

Supplementary data associated with this article can be found, in the online version, at doi:10.1016/j.bbrc.2012.01.155.

References

[1] M. Takano, R. Yumoto, T. Murakami, Expression and function of efflux drug transporters in the intestine, Pharmacol. Ther. 109 (2006) 137–161.
[2] J.R. Kunta, P.J. Sinko, Intestinal drug transporters: in vivo function and clinical importance, Curr. Drug. Metab. 5 (2004) 109–124.
[3] F. Thiebaut, T. Tsuruo, H. Hamada, M.M. Gottesman, I. Pastan, M.C. Willingham, Cellular localization of the multidrug-resistance gene product P-glycoprotein in normal human tissues, Proc. Natl. Acad. Sci. USA 84 (1987) 7735–7738.
[4] S. Hsing, Z. Gatmaitan, I.M. Arias, The function of Gp170, the multidrug-resistance gene product, in the brush border of rat intestinal mucosa, Gastroenterology 102 (1992) 879–885.
[5] M.F. Fromm, P-glycoprotein: a defense mechanism limiting oral bioavailability and CNS accumulation of drugs, Int. J. Clin. Pharmacol. Ther. 38 (2000) 69–74.
[6] R.B. Kim, M.F. Fromm, C. Wandel, B. Leake, A.J. Wood, D.M. Roden, G.R. Wilkinson, The drug transporter P-glycoprotein limits oral absorption and brain entry of HIV-1 protease inhibitors, J. Clin. Invest. 101 (1998) 289–294.
[7] G.Y. Kwei, R.F. Alvaro, Q. Chen, H.J. Jenkins, C.E. Hop, C.A. Keohane, V.T. Ly, J.R. Strauss, R.W. Wang, Z. Wang, T.R. Pippert, D.R. Umbenhauer, Disposition of ivermectin and cyclosporin A in CF-1 mice deficient in mdr1a P-glycoprotein, Drug Metab. Dispos. 27 (1999) 581–587.
[8] A. Sparreboom, J. van Asperen, U. Mayer, A.H. Schinkel, J.W. Smit, D.K. Meijer, P. Borst, W.J. Nooijen, J.H. Beijnen, O. van Tellingen, Limited oral bioavailability and active epithelial excretion of paclitaxel (Taxol) caused by P-glycoprotein in the intestine, Proc. Natl. Acad. Sci. USA 94 (1997) 2031–2035.
[9] J. van Asperen, O. van Tellingen, J.H. Beijnen, The role of mdr1a P-glycoprotein in the biliary and intestinal secretion of doxorubicin and vinblastine in mice, Drug Metab. Dispos. 28 (2000) 264–267.
[10] I.J. Hidalgo, T.J. Raub, R.T. Borchardt, Characterization of the human colon carcinoma cell line (Caco-2) as a model system for intestinal epithelial permeability, Gastroenterology 96 (1989) 736–749.
[11] J. Hunter, M.A. Jepson, T. Tsuruo, N.L. Simmons, B.H. Hirst, Functional expression of P-glycoprotein in apical membranes of human intestinal Caco-2 cells. Kinetics of vinblastine secretion and interaction with modulators, J. Biol. Chem. 268 (1993) 14991–14997.
[12] R. Yumoto, T. Murakami, Y. Nakamoto, R. Hasegawa, J. Nagai, M. Takano, Transport of rhodamine 123, a P-glycoprotein substrate, across rat intestine and Caco-2 cell monolayers in the presence of cytochrome P-450 3A-related compounds, J. Pharmacol. Exp. Ther. 289 (1999) 149–155.
[13] M. Takano, R. Hasegawa, T. Fukuda, R. Yumoto, J. Nagai, T. Murakami, Interaction with P-glycoprotein and transport of erythromycin, midazolam and ketoconazole in Caco-2 cells, Eur. J. Pharmacol. 358 (1998) 289–294.
[14] J.M. Dintaman, J.A. Silverman, Inhibition of P-glycoprotein by D-alpha-tocopheryl polyethylene glycol succinate (TPGS), Pharm. Res. 16 (1999) 1550–1556.
[15] H. van De Waterbeemd, D.A. Smith, K. Beaumont, D.K. Walker, Property-based design: optimization of drug absorption and pharmacokinetics, J. Med. Chem. 44 (2001) 1313–1333.
[16] I.J. Hidalgo, Assessing the absorption of new pharmaceuticals, Curr. Top. Med. Chem. 1 (2001) 385–401.
[17] T. Sato, R.G. Vries, H.J. Snippert, M. van de Wetering, N. Barker, D.E. Stange, J.H. van Es, A. Abo, P. Kujala, P.J. Peters, H. Clevers, Single Lgr5 stem cells build crypt-villus structures in vitro without a mesenchymal niche, Nature 459 (2009) 262–265.
[18] J.M. Croop, M. Raymond, D. Haber, A. Devault, R.J. Arceci, P. Gros, D.E. Housman, The three mouse multidrug resistance (mdr) genes are expressed in a tissue-specific manner in normal mouse tissues, Mol. Cell Biol. 9 (1989) 1346–1350.
[19] M.D. Perloff, E. Stormer, L.L. von Moltke, D.J. Greenblatt, Rapid assessment of P-glycoprotein inhibition and induction in vitro, Pharm. Res. 20 (2003) 1177–1183.
[20] J.S. Lee, K. Paull, M. Alvarez, C. Hose, A. Monks, M. Grever, A.T. Fojo, S.E. Bates, Rhodamine efflux patterns predict P-glycoprotein substrates in the National Cancer Institute drug screen, Mol. Pharmacol. 46 (1994) 627–638.
[21] P. Artursson, J. Karlsson, Correlation between oral drug absorption in humans and apparent drug permeability coefficients in human intestinal epithelial (Caco-2) cells, Biochem. Biophys. Res. Commun. 175 (1991) 880–885.
[22] D.C. Kim, P.S. Burton, R.T. Borchardt, A correlation between the permeability characteristics of a series of peptides using an in vitro cell culture model (Caco-2) and those using an in situ perfused rat ileum model of the intestinal mucosa, Pharm. Res. 10 (1993) 1710–1714.
[23] M.D. Ribadeneira, B.J. Aungst, C.J. Eyermann, S.M. Huang, Effects of structural modifications on the intestinal permeability of angiotensin II receptor antagonists and the correlation of in vitro, in situ, and in vivo absorption, Pharm. Res. 13 (1996) 227–233.
[24] B.H. Stewart, O.H. Chan, R.H. Lu, E.L. Reyner, H.L. Schmid, H.W. Hamilton, B.A. Steinbaugh, M.D. Taylor, Comparison of intestinal permeabilities determined in multiple in vitro and in situ models: relationship to absorption in humans, Pharm. Res. 12 (1995) 693–699.

Please cite this article in press as: T. Mizutani et al., Real-time analysis of P-glycoprotein-mediated drug transport across primary intestinal epithelium three-dimensionally cultured *in vitro*, Biochem. Biophys. Res. Commun. (2012), doi:10.1016/j.bbrc.2012.01.155

Cell

Leading Edge
Review

Autophagy: Renovation of Cells and Tissues

Noboru Mizushima[1,*] and Masaaki Komatsu[2,*]
[1]Department of Physiology and Cell Biology, Tokyo Medical and Dental University, Tokyo 113-8519, Japan
[2]Protein Metabolism Project, Tokyo Metropolitan Institute of Medical Science, Tokyo 156-8506, Japan
*Correspondence: nmizu.phy2@tmd.ac.jp (N.M.), komatsu-ms@igakuken.or.jp (M.K.)
DOI 10.1016/j.cell.2011.10.026

Autophagy is the major intracellular degradation system by which cytoplasmic materials are delivered to and degraded in the lysosome. However, the purpose of autophagy is not the simple elimination of materials, but instead, autophagy serves as a dynamic recycling system that produces new building blocks and energy for cellular renovation and homeostasis. Here we provide a multidisciplinary review of our current understanding of autophagy's role in metabolic adaptation, intracellular quality control, and renovation during development and differentiation. We also explore how recent mouse models in combination with advances in human genetics are providing key insights into how the impairment or activation of autophagy contributes to pathogenesis of diverse diseases, from neurodegenerative diseases such as Parkinson disease to inflammatory disorders such as Crohn disease.

All living organisms undergo continuous renovation. In humans, cells and intracellular components are constantly remodeled and recycled. This is, in part, in order to replace old components with fresh, better-quality ones. However, when components are replaced with different types, a net change in character results. Such "cellular renovation" requires synthesis of new components but also degradation of pre-existing materials, which can serve as building blocks.

Eukaryotic cells have two major degradation systems, the lysosome and the proteasome. Proteasomal degradation has high selectivity; the proteasome generally recognizes only ubiquitinated substrates, which are primarily short-lived proteins. By contrast, degradation in the lysosome does not follow such a simple pattern. Extracellular material and plasma membrane proteins can be delivered to lysosomes for degradation via the endocytic pathway. Furthermore, cytosolic components and organelles can also be delivered to the lysosome by autophagy (Figure 1).

The lysosome is often described as a "cellular garbage can," and its more positive roles in cellular renovation, particularly those involving autophagy, have not been well appreciated. In the 1990s, genetic studies in yeast identified a series of autophagy-related (*ATG*) genes (Klionsky et al., 2003; Nakatogawa et al., 2009). The results of these studies greatly increased our understanding of the mechanism and function of autophagy. In particular, analyses of autophagy-defective organisms have revealed numerous physiological and pathological roles of autophagy at both the cellular and whole-organism levels. In this Review, we summarize the current knowledge of autophagy and discuss the multidisciplinary function of autophagy in renovation of the cell and the organism.

Mechanisms of Autophagy

Autophagy is a generic term for all pathways by which cytoplasmic materials are delivered to the lysosome in animal cells or the vacuole in plant and yeast cells. There are roughly three classes of autophagy (Figure 1): macroautophagy, microautophagy, and chaperone-mediated autophagy. Macroautophagy uses the intermediate organelle "autophagosome." An isolation membrane (also termed phagophore) sequesters a small portion of the cytoplasm, including soluble materials and organelles, to form the autophagosome. The autophagosome fuses with the lysosome to become an autolysosome and degrade the materials contained within it. Autophagosomes may fuse with endosomes before fusion with lysosomes.

In microautophagy, the lysosome itself engulfs small components of the cytoplasm by inward invagination of the lysosomal membrane (Figure 1). Membrane dynamics during microautophagy may be quite similar or identical to that of endosomal sorting complex required for transport (ESCRT)-dependent multivesicular body (MVB) formation, which occurs in the late endosome. In fact, significant amounts of cytosolic proteins are incorporated into the endosomal lumen during MVB formation both in bulk and selectively (Sahu et al., 2011).

The third type of autophagy is chaperone-mediated autophagy. This class does not involve membrane reorganization; instead, substrate proteins directly translocate across the lysosomal membrane during chaperone-mediated autophagy (Figure 1). The chaperone protein Hsc70 (heat shock cognate 70) and cochaperones specifically recognize cytosolic proteins that contain a KFERQ-like pentapeptide (Orenstein and Cuervo, 2010). The transmembrane protein Lamp-2A, which is an isoform of Lamp-2, acts as a receptor on the lysosome, and unfolded proteins are delivered into the lysosomal lumen through a multimeric translocation complex.

Macroautophagy is thought to be the major type of autophagy, and it has been studied most extensively compared to microautophagy and chaperone-mediated autophagy. Therefore, herein we refer to macroautophagy simply as "autophagy."

Autophagy is highly inducible, with starvation and other stresses rapidly increasing the number of autophagosomes. Autophagosomes are generated on or in close proximity to the

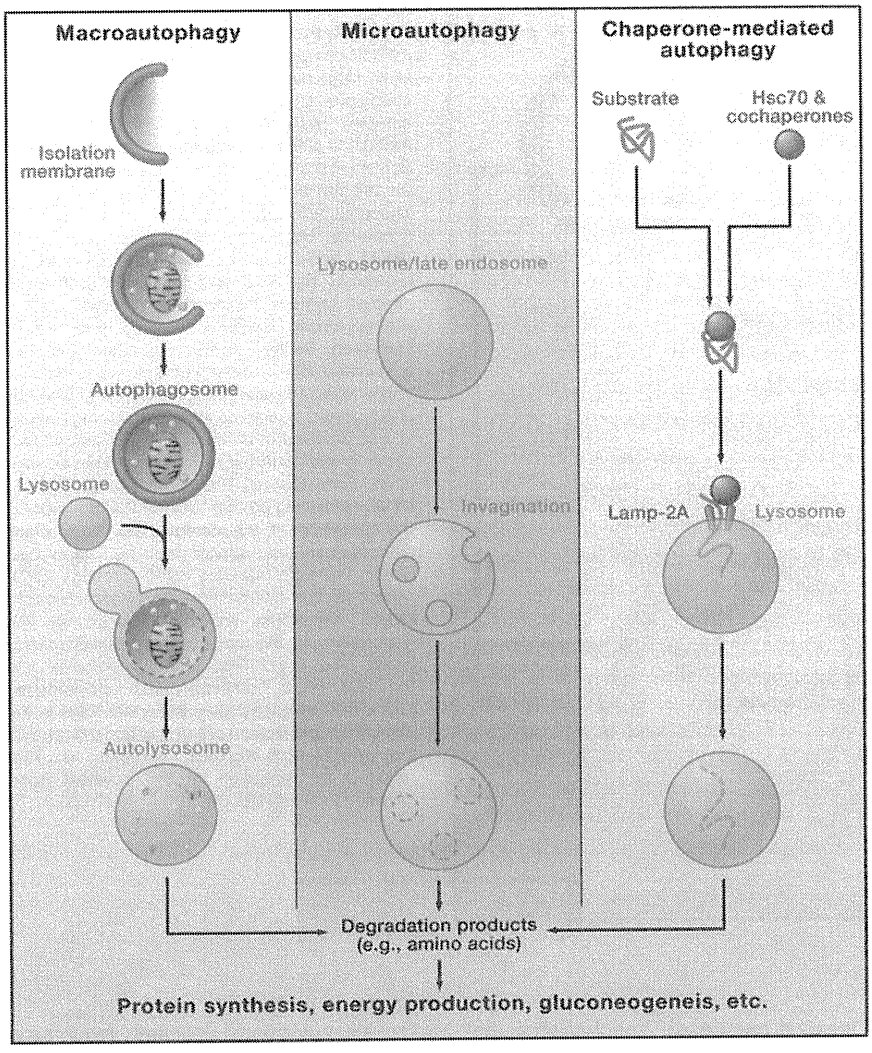

Figure 1. Different Types of Autophagy

Macroautophagy: A portion of cytoplasm, including organelles, is enclosed by an isolation membrane (also called phagophore) to form an autophagosome. The outer membrane of the autophagosome fuses with the lysosome, and the internal material is degraded in the autolysosome.

Microautophagy: Small pieces of the cytoplasm are directly engulfed by inward invagination of the lysosomal or late endosomal membrane.

Chaperone-mediated autophagy: Substrate proteins containing a KFERQ-like pentapeptide sequence are first recognized by cytosolic Hsc70 and cochaperones. Then they are translocated into the lysosomal lumen after binding with lysosomal Lamp-2A.

After all three types of autophagy, the resultant degradation products can be used for different purposes, such as new protein synthesis, energy production, and gluconeogenesis.

endoplasmic reticulum (ER) (Figure 2) (Mizushima et al., 2011; Tooze and Yoshimori, 2010). However, it remains unclear whether the ER membrane is directly used for autophagosome formation. Recent studies suggest that additional membranes derived from the Golgi complex, the mitochondria, and the plasma membrane also contribute to autophagosome formation (Hailey et al., 2010; Mizushima et al., 2011; Ravikumar et al., 2010; Tooze and Yoshimori, 2010). Thus, autophagosome formation likely involves multiple, complex processes.

Multiple Atg proteins govern autophagosome formation. Among the 35 Atg proteins thus far identified in yeast, Atg1–10, 12–14, 16, and 18 are the "core Atg proteins" (Nakatogawa et al., 2009). These proteins are required for autophagosome formation, in addition to Atg17, 29, and 31. The core Atg proteins are shared by other autophagy-related pathways, such as pexophagy (autophagic degradation of the peroxisome) and the cytoplasm-to-vacuole targeting pathway, which have been discussed in more detail in other reviews (Chen and Klionsky, 2011; Nakatogawa et al., 2009; Youle and Narendra, 2011).

The core Atg proteins are highly conserved in other eukaryotes, including mammals, and they act in a similar hierarchical manner in yeast and mammals (Itakura and Mizushima, 2010; Suzuki et al., 2007). Figure 2 summarizes their functional steps in mammalian cells, and more details for this process are described extensively elsewhere (Chen and Klionsky, 2011; Mizushima et al., 2011; Nakatogawa et al., 2009).

Adaptive Metabolic Response

The proteasome functions as a major generator of amino acids under normal nutrient-rich conditions, but autophagy's contribution to amino acid production increases when cells are starved (Vabulas and Hartl, 2005). Limitation of various types of nutrients, such as amino acids, growth factors, oxygen, and energy, can induce autophagy (He and Klionsky, 2009; Kroemer et al., 2010). Among these nutrients, starvation of nitrogen or amino acids induces the highest levels of autophagy in yeast and cultured mammalian cells, respectively. This is quite reasonable because the main products of autophagy are amino acids derived from cellular proteins. Restoration of cellular (or local) levels of amino acids reactivates the serine/threonine protein kinase mTORC1 (mammalian target of rapamycin complex 1) and terminates autophagy (Yu et al., 2010). Autophagy, therefore, constitutes a negative feedback loop in response to nutrient starvation.

When yeast cells are cultured in nitrogen-free medium, autophagy-deficient cells rapidly decrease intracellular amino acid levels (Onodera and Ohsumi, 2005) and lose their viability (Tsukada and Ohsumi, 1993). Similarly, mice with systemic deletion of *Atg3* (Sou et al., 2008), *Atg5* (Kuma et al., 2004), and *Atg7* (Komatsu et al., 2005) die immediately after birth and show reduced amino acid levels in tissues and plasma during the neonatal starvation period. Thus, enhanced degradation of

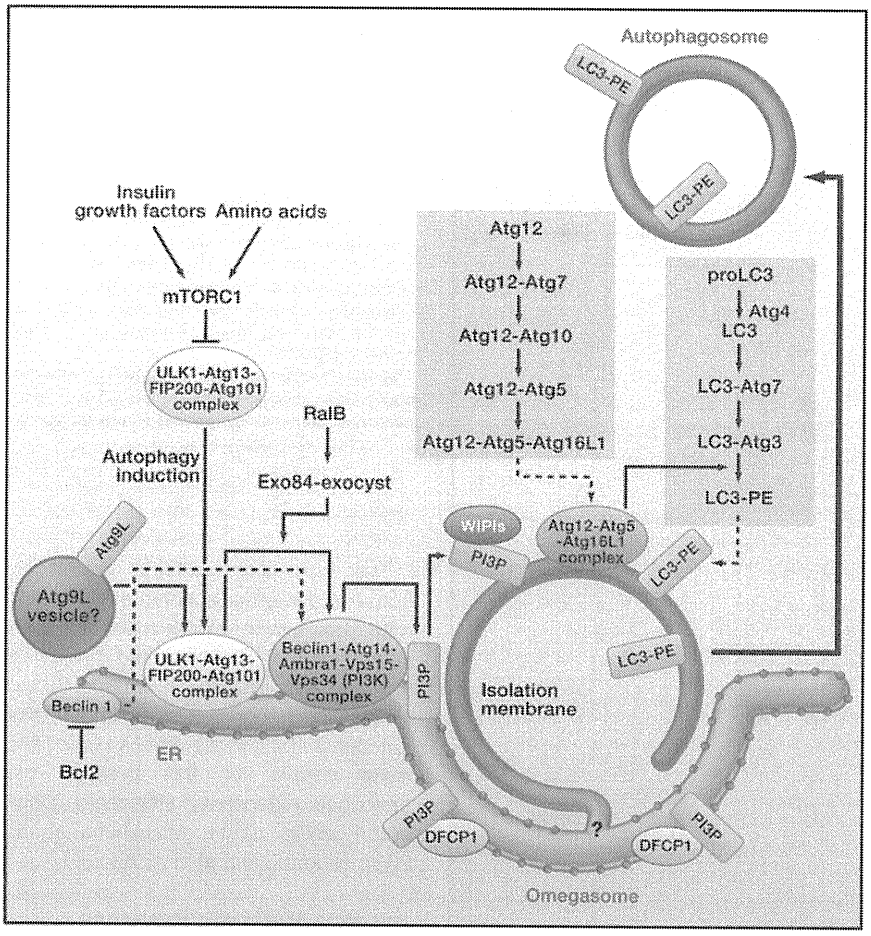

Figure 2. Autophagosome Formation and Atg Proteins in Mammalian Cells

mTOR complex 1 (mTORC1) suppresses the ULK1 (Atg1 homolog) complex under nutrient-rich conditions. Upon autophagy induction, the ULK1 complex (including ULK1, Atg13, FIP200, and Atg101) is activated and translocates to a certain domain of the endoplasmic reticulum (ER). Once in the ER, the ULK1 complex regulates the class III phosphatidylinositol (PtdIns) 3-kinase complex (including Beclin 1, Atg14(L)/barkor, Vps15, Vps34, and Ambra1), and this regulation is promoted by RalB and an Exo84-containing exocyst complex. Recruitment of Beclin 1 to the PtdIns3-kinase complex is also sensitive to starvation; Beclin 1 forms a complex with ER-associated Bcl-2 under nutrient-rich conditions and is released upon phosphorylation of Bcl-2 by JNK1. Atg9L, a multimembrane-spanning protein, is also involved in an early stage of autophagosome formation (Atg9L is recruited likely on vesicles). Formation of PtdIns(3)P recruits double FYVE-containing protein 1 (DFCP1) and promotes the formation of the omegasome, from which autophagosomes appear to be generated. Other PtdIns(3)P-binding WIPI proteins (WD-repeat protein interacting with phosphoinoside) (Atg18 homologs) are also crucial for the maturation of the omegasome/isolation membrane. The Atg12–Atg5–Atg16L1 complex and the LC3 (Atg8 homolog)–phosphatidylethanolamine (PE) conjugate play important roles in the elongation and closure of the isolation membrane. The Atg12–Atg5–Atg16L1 complex is also required for formation of the covalent bond between LC3 and PE.

self-components by autophagy is a critical survival response against starvation conditions.

An important question is, how do cells use these amino acids produced by autophagy (Figures 1 and 3)? Initial induction of autophagy is very rapid and occurs before energy fuels are completely exhausted. For instance, mice starved for 24 hr show increased autophagy in many tissues, but they still have sufficient lipids (glycogen may be consumed during the first day). Therefore, it is unlikely that autophagy simply supplies energy in these settings. In fact, several studies have suggested that autophagy-derived amino acids are used to synthesize proteins essential for starvation adaptation.

Protein anabolism is generally downregulated in starved cells, but synthesis of certain types of proteins continues or is even upregulated during starvation. These include vacuolar/lysosomal enzymes, respiratory chain proteins, antioxidant enzymes, and proteins involved in pathways of amino acid biosynthesis (Onodera and Ohsumi, 2005; Suzuki et al., 2011). Autophagy-deficient yeast cells fail to synthesize these proteins during starvation. As a result, these mutants loose respiratory function and accumulate higher levels of reactive oxygen species, which further decreases their mitochondrial DNA content (Suzuki et al., 2011). These appear to be the major mechanisms that rapidly kill autophagy-deficient yeast cells during nitrogen limitation.

Nonetheless, autophagy seems to be an important energy generator in certain settings. Amino acids can be converted into intermediates of the tricarboxylic acid (TCA) cycle and thus contribute to ATP production. Metabolome analysis of Ras-expressing cancer cells shows that autophagy is important for maintenance of TCA cycle metabolites (Guo et al., 2011). It is interesting that citrate, aconitate, and isocitrate, which are solely produced in mitochondria, are specifically reduced, suggesting that autophagy could be important not only for providing TCA metabolites but also for quality control of mitochondria. In addition, breakdown of lipid droplets by autophagy (lipophagy) may also account for its energy-producing role, especially in the liver (Singh et al., 2009).

Finally, amino acids are thought to be an important source for gluconeogenesis in the liver. In fact, when *Atg7* is deleted specifically in the liver, the mutant mice show reduced levels of blood glucose and amino acids after 24 hr of starvation (Ezaki et al., 2011). This finding suggests that amino acids generated inside the liver are used for gluconeogenesis and maintenance of the plasma pool of amino acids. How much autophagy contributes to overall gluconeogenesis is still unknown.

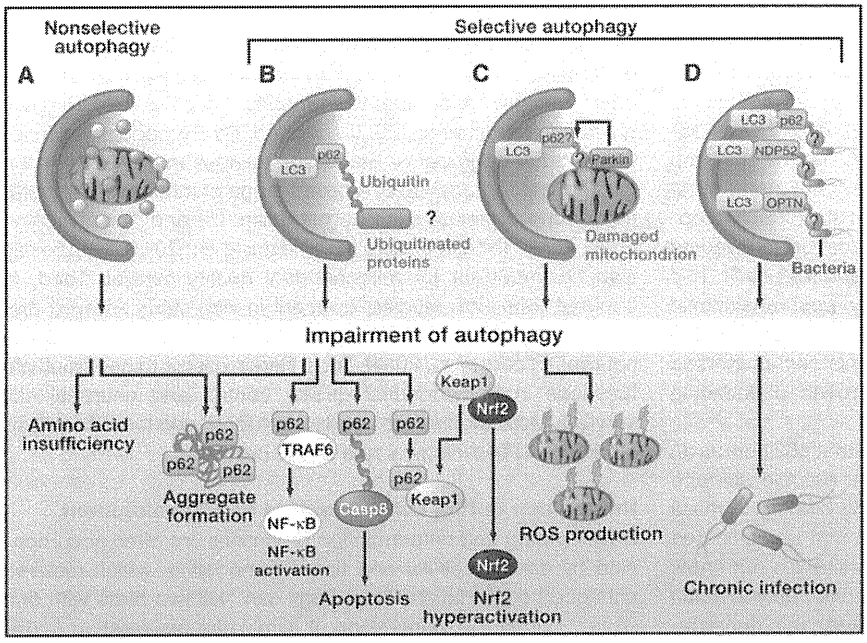

Figure 3. Nonselective and Selective Autophagy

(A) Upon nutrient deprivation, autophagy catabolizes cytoplasmic components nonselectively into building blocks, such as amino acids. A defect in this process causes amino acid insufficiency, which impairs protein synthesis for adaptation to starvation and energy production for cell survival. Autophagy also occurs constitutively at low levels even under nutrient-rich conditions and mediates global turnover of cytoplasmic materials.

(B) The LC3-binding protein p62 is a specific substrate for autophagy. Defective autophagy is usually accompanied by extensive accumulation of p62. This accumulation enhances p62's function as a scaffold protein in several signaling pathways, such as NF-κB signaling, apoptosis, and Nrf2 activation. p62 has a UBA domain through which it can mediate sequestration of ubiquitinated proteins into autophagosomes.

(C) In response to the loss of the mitochondrial membrane potential, Parkin translocates to damaged mitochondria in a PINK1-dependent manner and then ubiquitinates outer membrane proteins, which then induce mitophagy. The involvement of p62 as an adaptor is controversial. Mutants of *Parkin* and *PINK1*, which are associated with Parkinson disease, are unable to induce mitophagy, suggesting that the remaining damaged mitochondria have a role in the pathogenesis of Parkinson disease.

(D) Invading bacteria in the cytosol and/or ruptured endosomal membranes are ubiquitinated, and autophagic receptors including p62, NDP52, and optineurin mediate autophagic sequestration of the microbes to restrict their growth.

Intracellular Quality Control by Nonselective and Selective Autophagy

Approximately 1%–1.5% of cellular proteins are catabolized per hour by autophagy, even under nutrient-rich conditions in the liver. It is unclear how much basal autophagy contributes to macromolecule synthesis and energy production in the steady state by supplying amino acids, glucose, and free fatty acids. Nevertheless, basal autophagy acts as the quality-control machinery for cytoplasmic components, and it is crucial for homeostasis of various postmitotic cells, such as neurons and hepatocytes. Although this quality control could be partially achieved by nonselective autophagy, increasing evidence indicates that "selective" autophagy degrades specific proteins, organelles, and invading bacteria (Figure 3). Selective autophagy occurs constitutively and can also be induced in response to cellular stresses.

Selective Degradation of p62

One of the best characterized substrates of selective autophagy is p62, which is also known as sequestosome 1/SQSTM1. p62 is an ubiquitously expressed cellular protein, which is conserved in animals but not in plants and fungi. p62 directly interacts with LC3 (microtubule-associated protein light chain 3) on the isolation membrane through the LC3-interacting region (Figure 3). (LC3 is the mammalian homolog of Atg8 in yeast.) Subsequently, p62 is incorporated into the autophagosome and then degraded (Johansen and Lamark, 2011; Weidberg et al., 2011).

Impairment of autophagy is accompanied by accumulation of p62. This leads to the formation of large aggregates, which include p62 and ubiquitin (Komatsu et al., 2007a). Similar inclusion bodies with p62 and ubiquitin have been identified in various neurodegenerative diseases, including Alzheimer disease, Parkinson disease, and amyotrophic lateral sclerosis; liver disorders, including alcoholic hepatitis and steatohepatitis; and cancers, including malignant glioma and hepatocellular carcinoma (Zatloukal et al., 2002). When Atg7 is disrupted in livers and brains of mice, p62-positive aggregates are observed in their hepatocytes and neurons, respectively. Interestingly, these aggregates, as well those in human hepatocellular carcinoma cells, are completely dispersed by the additional loss of *p62* (Inami et al., 2011; Komatsu et al., 2007a). These findings implicate p62 in the formation of disease-related inclusion bodies (Figure 3).

p62 functions as a signaling hub that may determine whether cells survive by activating the TNF receptor-associated factor 6 (TRAF6)–NF-κB pathway or die by facilitating the aggregation of caspase-8 and downstream effector caspases (Moscat and Diaz-Meco, 2009). On the other hand, p62 interacts with the Nrf2-binding site on Keap1, a component of Cullin3-type ubiquitin ligase for Nrf2. This interaction stabilizes Nrf2 and activates the transcription of Nrf2 target genes, including a battery of antioxidant proteins (Komatsu et al., 2010; Lau et al., 2010). It is thus possible that excess accumulation or aggregation of p62 leads to hyperactivation of these signaling pathways (Figure 3).

Selective Degradation of Ubiquitinated Cargos

Almost all tissues with defective autophagy display an accumulation of polyubiquitinated proteins (Mizushima and Levine, 2010). Loss of autophagy is thought to delay global turnover of cytoplasmic components (Hara et al., 2006) and impair the degradation of substrates destined for the proteasome (Korolchuk et al., 2009). These effects could partially explain the accumulation of misfolded and unfolded proteins followed by the formation of inclusion bodies.

However, p62 has a ubiquitin-associated (UBA) domain. Thus, it has been proposed that p62 may be an autophagy receptor for degrading ubiquitinated cargos, including ubiquitinated aggregates, damaged mitochondria, ubiquitinated midbody rings, ubiquitin-tagged peroxisomes, ubiquitinated microbes, ribosomal proteins, and virus capsid proteins (Johansen and Lamark, 2011; Weidberg et al., 2011) (Figure 3). p62 and other adaptor proteins, such as NDP52 (Thurston et al., 2009) and optineurin (Wild et al., 2011), mediate the degradation of invading microbes via their interaction with ubiquitination (Figure 3). This selective autophagy could be regulated by posttranslational modification of the adaptors. For instance, TANK-binding kinase (TBK1) phosphorylates optineurin, which enhances its binding affinity to LC3 and thereby suppresses growth of invading microbes (Wild et al., 2011).

Although a large number of studies suggest that p62 acts as an ubiquitin adaptor, it is still unknown whether soluble ubiquitinated proteins are also degraded through p62 binding. A mass spectrometric analysis clearly demonstrated that ubiquitinated proteins in autophagy-deficient livers and brains do not show any linkage specificity, indicating that specific polyubiquitin chain linkage is not the decisive signal for autophagic degradation (Riley et al., 2010). The simultaneous knockout of either *p62* or *Nrf2* completely suppresses the increase in ubiquitin conjugates in *Atg7*-deficient liver and brain (Riley et al., 2010). Therefore, the accumulation of ubiquitinated proteins in tissues defective in autophagy might be attributed to p62-mediated activation of Nrf2, resulting in global transcriptional changes to ubiquitin-associated genes. Further studies will be needed to elucidate more precisely the mechanism of degradation of ubiquitinated proteins by autophagy.

Degradation of Damaged Mitochondria: Implications for the Pathogenesis of Parkinson Disease

Recent studies have described the molecular mechanism by which damaged mitochondria are selectively targeted for autophagy, and these studies also suggest that the defects in this process underlie familial Parkinson disease (Youle and Narendra, 2011). PINK1, a mitochondrial kinase, and Parkin, an E3 ubiquitin ligase, have been genetically linked to both Parkinson disease and a pathway that prevents progressive mitochondrial damage and dysfunction. When mitochondria are damaged and depolarized, PINK1 becomes stabilized and recruits Parkin to the damaged mitochondria (Matsuda et al., 2010; Narendra et al., 2008; Narendra et al., 2010a; Vives-Bauza et al., 2010). Parkin ubiquitinates various mitochondrial outer membrane proteins, which could trigger mitophagy. However, the precise substrate of Parkin, which is essential for mitophagy, is still unknown (Figure 3). Of note, mutations in *PINK1* and *Parkin*, which are associated with Parkinson disease, are known to impair mitophagy (Matsuda et al., 2010; Narendra et al., 2008, 2010a; Vives-Bauza et al., 2010), suggesting that there is a link between defective mitophagy and Parkinson disease. Accumulation of damaged mitochondria would cause oxidative stress and loss of neuronal cells.

Nevertheless, many questions remain about mitophagy and Parkin. First, it is unknown how the autophagosome recognizes these ubiquitinated mitochondria. Although p62 has been implicated in this recognition process, elimination of mitochondria occurs normally in *p62*-deficient cells (Narendra et al., 2010b; Okatsu et al., 2010). p62 seems to be required for the clustering of depolarized mitochondria in the perinuclear region. The role of other mitochondrial adaptor proteins such as Nix remains unknown (Novak et al., 2010). Second, Parkin appears to function in other degradative processes besides mitophagy. Parkin can induce degradation of a broad range of mitochondrial outer membrane proteins, such as mitofusin 1/2 and Tom20 (Chan et al., 2011; Tanaka et al., 2010; Yoshii et al., 2011), which may also be important for mitochondrial quality control. Third, in contrast to in vitro studies, a recent in vivo study showed that depolarized mitochondria do not recruit Parkin in dopamine neurons (Sterky et al., 2011). Thus, Parkin seems to have multiple functions in mitochondrial quality control and neuronal cell survival. More studies are needed to fully understand the physiological and pathological role of this protein.

Renovation during Differentiation and Development

Development and differentiation processes are often accompanied by drastic cellular and tissue remodeling, which requires enhanced degradation. Autophagy can "kill two birds with one stone" during this remodeling; it eliminates pre-existing materials and provides support for the subsequent creation of new components (Mizushima and Levine, 2010). For example, autophagy has been shown to be required for formation of spores in yeast (Tsukada and Ohsumi, 1993) and dauer larvae in *Caenorhabditis elegans* (Meléndez et al., 2003), both of which are triggered by starvation to sustain the organism during adverse conditions. Autophagy also plays a crucial role in insect metamorphosis (Ryoo and Baehrecke, 2010). It is possible that autophagy-derived amino acids can be used as essential building blocks in these processes.

The most dramatic cellular renovation may occur shortly after fertilization. Maternal proteins and messenger RNAs (mRNAs) are extensively degraded while new proteins encoded by the zygotic genome are synthesized. In mammals, fertilization induces massive autophagy, which plays an essential role in early embryogenesis (Tsukamoto et al., 2008) (Figure 4). Nutrient availability may be limited in embryos until implantation, and autophagy functions as a major nutrient-providing system during this period. In addition, autophagy in early embryos is essential for selective elimination of paternal mitochondria in *C. elegans*. This could be a key mechanism underlying maternal inheritance of mitochondrial DNA and may be conserved in mammals (Sato and Sato, 2011; Al Rawi et al., 2011).

Atg3$^{-/-}$ (Sou et al., 2008), *Atg5*$^{-/-}$ (Kuma et al., 2004), *Atg7*$^{-/-}$ (Komatsu et al., 2005), *Atg9*$^{-/-}$ (Saitoh et al., 2009), and *Atg16L1*$^{-/-}$ (Saitoh et al., 2008) mice die shortly after birth without apparent anatomical abnormalities. However, tissue-specific gene-targeting studies have later revealed that autophagy functions in several specific lineages of differentiation, such as adipocytes, erythrocytes, T cells, and B-1a cells (Figure 4). Autophagy may play an important role in complete or partial elimination of mitochondria during these processes (Mizushima and Levine, 2010). In a separate mechanism, autophagy in thymic epithelial cells could be involved in the establishment of self-tolerance of T cells; specifically, autophagy fine tunes epithelial cells' presentation of self-antigens to